國立臺灣大學電機資訊學院電信工程學研究所

碩士論文

Graduate Institute of Communication Engineering

College of Electrical Engineering and Computer Science

National Taiwan University

Master Thesis

跳頻及頻域分集多輸入多輸出雷達於假目標干擾下之目標偵測和定位

Frequency-Hopping Frequency-Diverse MIMO Radar for Target Detection and Localization under False-Target Jamming

辛佳亮

Chia-Liang Hsin

指導教授：江簡富 博士

Advisor: Jean-Fu Kiang, Ph.D.

中華民國 112 年 7 月

July 2023

doi:10.6342/NTU202302364

Acknowledgment

First of all, I would like to express my sincerest thanks to my thesis advisor, Professor Jean-Fu Kiang, for his advices and supports throughout the past two years to pursue my master degree. His exciting lectures, enthusiastic attitude, and research experiences motivate me to enhance my understanding on electromagnetic theories and their applications. I am also grateful to my thesis readers, Professor Jian-Jiun Ding and Professor Hsiang-Chieh Lee for their valuable comments to improve the quality of this thesis. I would like to thank the faculty in the Department of Electrical Engineering and the Graduate Institute of Communication Engineering, Nation Taiwan University for many useful courses they offered. My classmates and friends in the graduate school are also appreciated for their friendship in these two years. The deepest appreciations are owed to my parents for their considerations and encouragement. They always support me to pursue this master degree, and I am pleased to share this honor with them.

doi:10.6342/NTU202302364

中文摘要

本論文提出一種新型 FH-LFM-FD-MIMO 雷達系統來檢測和定位真實目標，同時抑制虛假目標干擾信號。由發射陣列發射經過載波頻率優化的線性調頻 (LFM) 脈衝，來實現頻率分集多輸入多輸出（FD-MIMO）和跳頻（FH）方法。結合粒子群優化（PSO）算法和排序值（ROV）映射來生成頻率分集 (FD) 碼，以增強干擾抑制性能為目標，再依據頻率分集 (FD) 碼設定所有發射陣列單元的頻率偏移。應用特定的 FD 碼來實現跳頻（FH）方法，脈衝重複間隔可抑制頻域和空間域中的干擾信號，接收器檢測到具匹配 FD 代碼的目標回波，同時抑制具不匹配 FD 碼的假目標干擾信號。再使用第二種 PSO 算法優化聚焦範圍波束形成向量，以實現低旁辮的聚焦響應。檢測到目標後，應用二維最小方差無失真響應（2D-MVDR）以更精確地定位目標。提出一種二元積分檢測方法來增強嚴重干擾條件下的檢測性能。模擬結果驗證了所提出的 FH-LFM-FD-MIMO 雷達系統與傳統方法相比可以將輸出信號干擾加噪聲比（SJNR）提高 20 dB 以上，在給定誤報率下獲得更高的檢測機率，並提高定位精確度。

關鍵字: 跳頻、線性調頻脈衝、頻率分集多輸入多輸出、虛假目標干擾、聚焦響應、偵測、定位

doi:10.6342/NTU202302364

Abstract

A novel FH-LFM-FD-MIMO radar system is proposed to detect and localize true targets while suppressing false-target jamming signals. Linear frequency modulated (LFM) pulses are transmitted by a transmit array, with the carrier frequencies optimized to implement frequency-diverse multiple-input-multiple-output (FD-MIMO) and frequency-hopping (FH) schemes. The frequency offsets at all the transmit-array elements are represented as a frequency-diverse (FD) code, which is generated by combining a particle swarm optimization (PSO) algorithm and a rank-order-value (ROV) mapping to enhance the jamming suppression performance. The frequency-hopping (FH) scheme is implemented by applying specific FD codes in different pulse repetition intervals to suppress jamming signals in both frequency domain and spatial domain. The target echoes carrying matched FD code are detected at the receiver, while the false-target jamming signals carrying mismatched FD codes are suppressed. A spotlight response with low sidelobe level is achieved by optimizing the spotlight-range beamforming vector with a second PSO algorithm. After a target is detected, a two-dimensional minimum-variance distortionless response (2D-MVDR) is applied to pin-

doi:10.6342/NTU202302364

point the target with higher precision. A binary integration detection scheme is proposed to enhance the detection performance under more severe jamming condition. The simulation results verify that the proposed FH-LFM-FD-MIMO radar system can increase the output signal-to-jamming-plus-noise ratio (SJNR) by more than 20 dB compared to conventional approaches, acquiring higher probability of detection under constant false alarm rate and enhancing the localization precision.

Keywords: Frequency-hopping, linear frequency modulated (LFM) pulse, frequency-diverse multiple-multiple-output (FD-MIMO), false target jamming, spotlight response, detection, localization

doi:10.6342/NTU202302364

Contents

doi:10.6342/NTU202302364

doi:10.6342/NTU202302364

List of Figures

doi:10.6342/NTU202302364

doi:10.6342/NTU202302364

Chapter 1

Introduction

False-target jamming is often used to divert the opponent from detecting the true target [1]-[3]. The jamming signal can be generated by using a false target generator (FTG) equipped with digital radio frequency memory (DRFM) [4],[5]. The FTG intercepts the radar signals and then re-transmits their replica at specific delay, mimicking targets at false positions [6],[7]. False-target jamming is typically countered by enhancing the echoes from true targets while suppressing the echoes from false targets [8]-[10].

An FTG requires at least one acting radar signal for duplication and mimicking [11]-[14]. By casting some unique signature on each transmitted signal in different pulse repetition intervals (PRIs), the echoes from the true targets and the jamming signals can be differentiated. The signature can be cast in time, frequency or other domains. Pulse or waveform diversity is implemented in the time domain. In [15], the chirp rate of LFM signal was changed in each pulse repetition interval. In [16],[17], different waveforms were transmitted

doi:10.6342/NTU202302364

in different PRIs, hence the jamming signals could be eliminated by waveform matching at the receiver.

Frequency hopping or frequency agility is implemented in the frequency domain. In [18], a frequency agile radar (FAR) randomly changed its carrier frequencies in each PRI. In [19],[20], the carrier frequency and inter-pulse interval were varied from pulse to pulse, preventing the jammers from generating false signals at right carrier frequency. In [21], an extra phase modulation was imposed on each element and was changed from pulse to pulse, so that the true target and jammers can be separated in the spatial-frequency domain.

Spatial separation has been exploited to separate true targets from false ones. False targets can be generated to fulfill azimuth deception or mainlobe deception. An azimuth deception is usually achieved by transmitting signal to the sidelobe of the victim radar, making believe that a jammer appears in the mainlobe direction [22]. Sidelobe blanking [23] and sidelobe cancelation [24] were proposed to determine if the signal arrived from the mainlobe or sidelobe direction, followed by suppressing the jamming signals.

Data fusion based on a distributed multi-radar network could be used to recognize the scattering properties of targets and jammers. A typical target manifests specific bistatic scattering pattern, which is difficult to duplicate by a deceptive jammer [25]. In [26], the recognition task was reduced to a minimum-distance problem in terms of the target scattering

doi:10.6342/NTU202302364

signal and the jamming signal.

As for the mainlobe deception scheme, a false target can be generated in the same azimuth but different ranges from the target. A frequency diverse (FD) array can produce a spotlight beampattern by tuning frequency offsets across its array elements [27],[28], which is suitable for countermeasuring azimuth and mainlobe deception schemes. The diversity gain endowed provided by MIMO array and the range-azimuth-dependent feature of FD array are combined to form an FD-MIMO array [29]-[31], which can spotlight the target at specific range-azimuth cell and suppress jamming signals from other cells.

The frequency offsets have been tuned in terms of linear function [32], logarithmic function [33], symmetrical logarithmic function [34], Hamming window [35], and Taylor window [36]. Many optimization techniques have been proposed to generate a more focused beampattern with lower sidelobe level, including convex optimization [37], second-order cone programming [38], genetic algorithm [39], and particle swarm optimization [40].

The spotlight pattern of an FD-MIMO array can suppress range-dependent jamming or interference more effectively than conventional MIMO arrays. In [41], FD technique was combined with space-time adaptive processing (STAP) to form an FD-STAP radar for detecting fast-moving target and increasing the signal-to-interference-plus-noise ratio (SINR). Various methods on FD-MIMO arrays were proposed to detect target under Gaussian-like

doi:10.6342/NTU202302364

interference. In [42], an adaptive detector for FD-MIMO radar was implemented on a generalized likelihood ratio test (GLRT) criterion. In [43], a detector based on two-step GLRT was proposed to operate at constant false alarm rate. In [44], structured and unstructured GLRT based on Bayesian inference was introduced. Detection schemes could also be based on Rao test or Wald test [45],[46]. In [47], an FD-MIMO array was proposed to identify moving targets immersed in clutter by exploiting the azimuth, range and Doppler information. In [48], a cognitive FD-MIMO radar was proposed to detect moving targets by adaptively maximizing the SINR. The FD-MIMO arrays were shown to achieve better target detection performance than FD, MIMO or phased arrays [49].

In terms of target localization, various novel methods based on MIMO radar have been proposed to estimate direction-of-departure (DoD) and direction-of-arrival (DoA) of targets in recent years. In [50], a sparse L-shaped electromagnetic vector sensor (EMVS) MIMO radar was proposed for 2D-DoD and 2D-DoA estimation, and a two-step algorithm was designed to acquire unambiguous angle estimation with high accuracy. In [51], the conventional multiple signal classification (MUSIC) was combined with a scale discrete Fresnel transform (SDFnT) to form SDFnT-MUSIC, which was used to improve the accuracy of angle estimation. In [52], a max-MUSIC was proposed to estimate the DoA with high accuracy and without spatial aliasing, by constructing multiple subarrays from a sparse MIMO radar.

doi:10.6342/NTU202302364

In contrast to DoD and DoA estimation aimed for azimuth-angle estimation, FD-MIMO is capable of estimating both target range and azimuth angle. In [53], an FD-MIMO technique was proposed to extend the conventional MUSIC to the range-angle domain. In [54], a true target was localized with an FD-MIMO technique in the range-angle-Doppler domain, in the presence of false-target jamming signal. In [55], the MVDR spectrum for FD-MIMO was derived to perform joint range-angle estimation, with the simulated localization accuracy approaching the Cramér-Rao bound (CRB).

However, the pattern of an FD-MIMO array varies with time, and the transmitting waveforms are not orthogonal. Time-variant frequency offsets were proposed to generate stationary pattern [56]-[58], but was not successful [59],[60]. In [61]-[63], multiple bandpass filters and mixers were utilized to remove time dependency from the pattern, which will be incorporated into the proposed radar system. In [64], [65], multiple matched filters were applied to eliminate the time-variant term.

The orthogonality of waveforms achieved with conventional MIMO receiver was practically unattainable at all Doppler-delay instances [66]. It was impractical to extend the orthogonality assumption to some FD-MIMO applications [55], [67], [68]. Instead, waveforms with good auto-correlation and cross-correlation properties can be attained. In [69]-[71], phase-coded sequences were optimized with cyclic algorithms to generate waveforms

doi:10.6342/NTU202302364

with good correlation properties. An alternative to achieve orthogonality is through proper choice of frequency offsets. The orthogonality condition in [72] is adopted in this work. LFM pulse of duration T is chosen as the baseband waveform, the frequency offset between any two of the transmit-array elements is a non-zero integer multiply of $1/T$.

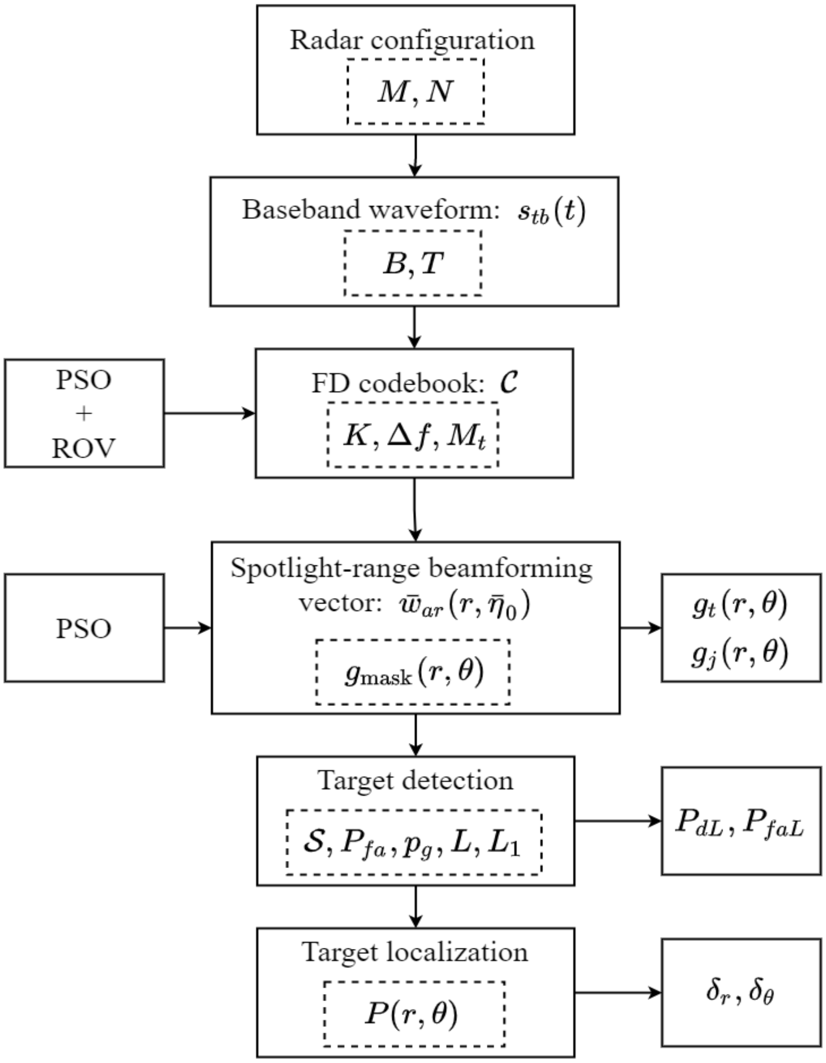

Figure 1.1: The block diagram that highlights series of steps of the proposed approach. The key parameters related to the step are enclosed by the dashed box.

In this work, we propose an FH-LFM-FD-MIMO radar by applying a frequency-hopping

doi:10.6342/NTU202302364

(FH) scheme to an FD-MIMO array, to detect and localize true targets while suppressing false-target jamming signals. Fig.1.1 shows the block diagram of steps in the proposed approach. The radar configuration and baseband waveform are decided first. Then, the FD codebook is generated by combining a particle swarm optimization (PSO) algorithm and a rank-order-value (ROV) mapping. For each FD code in the codebook, a corresponding spotlight-range beamforming vector is obtained with a second PSO algorithm to create low-sidelobe spotlight response for target detection and localization.

By exploiting the disparity between target echo and jamming signals in frequency and spatial domains, the target echo can be extracted and the jamming signals are significantly suppressed. Each of the transmit-array element in the FH-LFM-FD-MIMO array emits signal at a specified carrier frequency, which is properly offset from the reference frequency via a frequency offset index (FOI), as illustrated in Fig.2.2. The frequency offset indices (FOIs) applied across the whole transmit array are stored in a vector, called frequency-diverse (FD) code. The frequency-hopping (FH) scheme is implemented by applying different FD codes in different pulse repetition intervals. The FD codebook, FH sequence and the baseband waveform need to be orchestrated at the transmit and receive arrays, as illustrated in Fig.2.1.

The jamming signals emitted from a false-target generator are presumed to be replica of acting FD codes. The target echoes carrying matched FD codes are detected at the re-

doi:10.6342/NTU202302364

ceiver, as illustrated in Fig.2.3, while the jamming signals carrying mismatched FD codes are suppressed. In this work, the FD codes are designed by using a particle swarm optimization (PSO) method via a rank-order-value (ROV) mapping. The optimized FD codes are compiled to an FD codebook, in which each FD code is assigned an integer index. The sequential order of dispatching the FD codes to the arrays is recorded as an FH sequence. The generation of FD codebook is illustrated in the flow-chart of Fig.3.1.

A spotlight pattern on specific range-azimuth cell is achieved via the endowed properties of an FD-MIMO array. Phase adjustment at the receive-array elements is implemented by using a second PSO algorithm, as shown in Fig.4.1, to further focus the spotlight pattern. Finer range resolution is achieved by using linear frequency modulated (LFM) pulses than continuous-wave (CW) pulses. With the sharp spotlight pattern response of the proposed FH-LFM-FD-MIMO radar, the signal-to-jamming-plus-noise ratio (SJNR) is significantly increase, leading to much better detection probability under a constant false alarm rate. A binary integration detector approach is incorporated to suppress jamming signals that accidentally carry identical FD code to the target echo. A two-dimensional minimum-variance distortionless response (2D-MVDR) spectrum is used to pinpoint the target location at high precision within the target range-azimuth cell.

The rest of this paper is organized as follows. The signal model of FH-LFM-FD-MIMO

doi:10.6342/NTU202302364

is presented in Section II, the design of FD codebook is presented in Section III, the beamforming approach to achieve spotlight response is given in Section IV, the detection and localization algorithms are presented in Section V, and simulation results are discussed in Section VI. Finally, some conclusions are drawn in Section VII.

In this work, a variable with single bar ($\bar{w}$) indicates a vector, a variable with double bars ($\bar{\bar{h}}$) indicates a matrix. The symbols $\bar{0}_{MN}$, $\bar{I}_{MN}$ and $\bar{\bar{I}}_{MN\times MN}$ denote an $MN \times 1$ zero vector, an $MN \times 1$ all-one vector and an $MN \times MN$ identity matrix, respectively. The conjugate, transpose and conjugate transpose of a variable, vector or matrix $[\bullet]$ are denoted as $[\bullet]^*$, $[\bullet]^t$ and $[\bullet]^\dagger$, respectively. The Kronecker operator and Hadamard operator are denoted by $\otimes$ and $\odot$, respectively. $\mathrm{Re}\,\{z\}$ denotes the real part of z, $\mathrm{E}\,\{z\}$ denotes the expectation value of z, $\|\bullet\|$ denotes the two-norm of vector or matrix $\bullet$, $\mathcal{F}\{\bullet\}$ and $\mathcal{F}^{-1}\{\bullet\}$ denote the Fourier transform and inverse Fourier transform, respectively, of variable $\bullet$.

For convenience to the readers, all the symbols and definitions used in this work are listed in Table 1.1 in an alphabetical order (English symbols first, followed by Greek symbols), accompanied with the location of their first appearance.

Table 1.1: Symbols and definitions used in this work.

Symbol	Definition	Location
$\bar{a}(r,\theta,\bar{\eta},r',\theta',\bar{\eta}')$	transmit-array steering vector	(2.21)
$\bar{a}_r(r',\bar{\eta})$	transmit-range steering vector	(2.22)
$\bar{a}_\theta(\theta')$	transmit-azimuth steering vector	(2.23)
B	sweep bandwidth of $s_{tb}(t)$	(2.2)
$\bar{b}(\theta')$	receive-azimuth steering vector	(2.20)
$\mathcal{C}$	frequency-diverse (FD) codebook	Fig.2.1, (2.1)
f_0	reference frequency	Fig.2.2, (2.5)
$g_0(r,\theta)$	normalized spotlight response	(4.3)
$g_j(r,\theta)$	average normalized response to jamming signal	(4.14)
$g_{\text{mask}}(r,\theta)$	normalized response mask	(4.9)
$g_t(r,\theta)$	average normalized response to target	(4.13)
$\bar{h}(t,\bar{\eta},\bar{\eta}')$	code-matching matrix	(2.16), (2.21)
K	number of FD codes in $\mathcal{C}$	(2.1)
k_0	wavenumber corresponding to f_0	Fig.2.2, (2.15)
M	number of transmit array elements	Fig.2.1
M_t	maximum integer a FOI can be	(2.5),
N	number of receive array elements	Fig.2.1
P_d	average detection probability over all FD code in single trial	(5.18)
P_{dL}	overall detection probability after L_1-of-L binary integration	(5.21)
P_{fa}	false alarm rate in single trial	(5.15)
P_{faL}	overall false alarm rate after L_1-of-L binary integration	(5.22)
$P(r,\theta)$	2D-MVDR spectrum	(5.24)
Q	number of false-target jamming signals	(2.7)
r_q	range of the qth signal in received signal	(2.8), (2.9)

doi:10.6342/NTU202302364

Symbol	Definition	Location
$\mathcal{S}$	frequency-hopping (FH) sequence	Fig.2.1
$s_{bn}(t,\theta)$	$s_n(t,\theta)$ in baseband	Fig.2.3, (2.12)
$s_{bqn}(t,\theta)$	$s_{qn}(t,\theta), q = 0, 1, \cdots, Q$ in baseband	(2.12)
$s_n(t,\theta)$	received signal at the receive array	Fig.2.3, (2.7)
$s_{tb}(t)$	baseband waveform	Fig.2.1, (2.3)
$s_{tm}(t,\theta)$	the transmitted signal of the mth transmit-array element	Fig.2.2, (2.2)
$s_{qn}(t,\theta)$	the qth ($q = 0, 1, \cdots, Q$) signal component of $s_n(t,\theta)$	(2.8)
T	duration of $s_{tb}(t)$	(2.2)
$u(t,\theta,\bar{\eta}_0)$	result of applying spotlight beamforming vector to $\bar{v}(t,\theta,\bar{\eta}_0)$	(2.28)
$u_q(t,\theta,\bar{\eta}_0)$	the qth ($q = 0, 1, \cdots, Q$) signal component of $u(t,\theta,\bar{\eta}_0)$	(2.28)
$\bar{v}(t,\theta,\bar{\eta}_0)$	received signal vector after matched filtering	(2.24)
$\bar{v}_q(t,\theta,\bar{\eta}_0)$	the qth ($q = 0, 1, \cdots, Q$) signal component of $\bar{v}(t,\theta,\bar{\eta}_0)$	(2.17)
$\bar{w}(r,\theta,\bar{\eta}_0)$	spotlight beamforming vector	(2.25)
$\bar{w}_{ar}(r,\bar{\eta}_0)$	spotlight-range beamforming vector	(2.25)
$\bar{w}_{a\theta}(\theta)$	transmit-azimuth beamforming vector	(2.6)
$\bar{w}_b(\theta)$	spotlight-azimuth beamforming vector	(2.25)
α_q	amplitude of the qth signal in received signal	(2.8)
Δf	frequency step	Fig.2.2, (2.5)
$(\delta r)^2$	CRB on range	(5.36)
$(\delta\theta)^2$	CRB on azimuth	(5.37)
η_m	frequency offset index of the mth transmit-array element	Fig.2.2, (2.5)
$\bar{\eta}_q$	FD code of target ($q = 0$) or jamming signal ($q = 1, \cdots, Q$)	(2.8)
θ_q	azimuth of the qth signal in received signal	(2.8), (2.9)

doi:10.6342/NTU202302364

Chapter 2

Signal Model

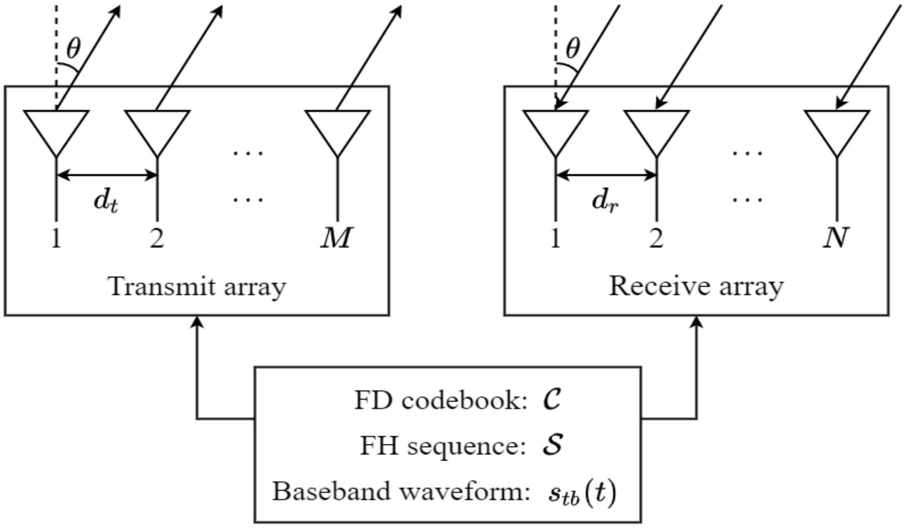

Figure 2.1: Configuration of co-located FH-LFM-FD-MIMO radar.

Fig.2.1 shows the configuration of the proposed FH-LFM-FD-MIMO radar, where the co-located transmit array and receive array are composed of M and N elements, respectively, with the inter-element spacings of d_t and d_r, respectively. The FD codebook $\mathcal{C}$ is a composed of K FD codes,

$$\mathcal{C} = \{\bar{c}_1, \bar{c}_2, \cdots, \bar{c}_K\} \tag{2.1}$$

doi:10.6342/NTU202302364

where $\bar{c}_k = [c_{k1}, c_{k2}, \cdots, c_{kM}]^t$ and the superscript t denotes a transpose operator. The FH sequence $\mathcal{S}$ is a sequence of integers between 1 and K. One FD code index is read from the FH sequence in each pulse repetition interval, and the carrier frequencies of the transmit-array elements are determined according to the FD code.

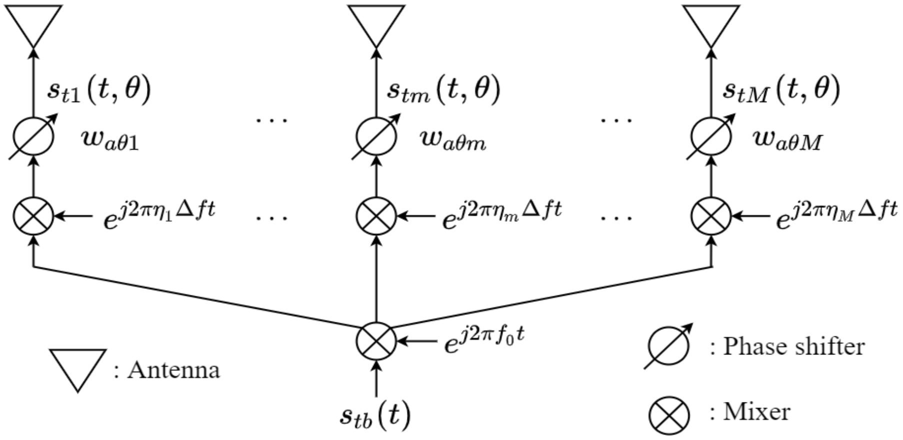

Figure 2.2: Schematic of transmit array.

Fig.2.2 shows the transmit array of the FH-LFM-FD-MIMO radar. The transmitted signal of the mth ($m = 1, 2, \cdots, M$) transmit-array element is given by

$$s_{tm}(t,\theta) = w_{a\theta m} s_{tb}(t) e^{j2\pi f_m t} \tag{2.2}$$

where f_m and $w_{a\theta m}$ are the carrier frequency and the weighting, respectively, of the mth transmit-array element, and $s_{tb}(t)$ is the baseband waveform of an LFM pulse,

$$s_{tb}(t) = \sqrt{\frac{E}{T}} e^{j\pi(B/T)t^2} \mathrm{rect}(t/T) \tag{2.3}$$

where E is the energy radiated from an antenna element in a PRI, B is the bandwidth of the LFM pulse, T is the pulse length, and $\mathrm{rect}(t/T)$ is a window function, with

$$\mathrm{rect}(\tau) = \begin{cases} 1, & |\tau| \leq 1/2 \\ 0, & \text{otherwise} \end{cases} \tag{2.4}$$

The carrier frequency f_m is given by

$$f_m = f_0 + \eta_m \Delta f, \quad m = 1, \cdots, M \tag{2.5}$$

where f_0 is the reference frequency, $\Delta f = 1/T$ is frequency spacing [72], η_m is an integer frequency offset index (FOI), with $0 \leq \eta_m \leq M_t$, and M_t is the maximum allowable FOI. The FOIs assigned to all the transmit-array elements in a pulse repetition interval are stored in an FD code $\bar{\eta} = [\eta_1, \eta_2, \cdots, \eta_M]^t \in \mathcal{C}$. For example, if $\bar{\eta} = \bar{c}_k$, then $f_m = f_0 + c_{km}\Delta f$. To steer the beam of transmit array towards the azimuth of θ, a phase $w_{a\theta m} = e^{jk_0 d_t (m-1)\sin\theta}$ is imposed to the mth element, with $m = 1, \cdots, M$, where $k_0 = 2\pi/\lambda_0$ is the wavenumber at the reference frequency f_0. These phase terms are stored in a transmit-azimuth beamforming vector as

$$\bar{w}_{a\theta}(\theta) = [w_{a\theta 1}, w_{a\theta 2}, \cdots, w_{a\theta M}]^t. \tag{2.6}$$

Fig.2.3 shows the receive array of the FH-LFM-FD-MIMO radar. Assume there are one true target and Q false-target jamming signals, the received signal at the nth receive-array element is given by

$$s_n(t,\theta) = s_{0n}(t,\theta) + \sum_{q=1}^{Q} s_{qn}(t,\theta) \tag{2.7}$$

doi:10.6342/NTU202302364

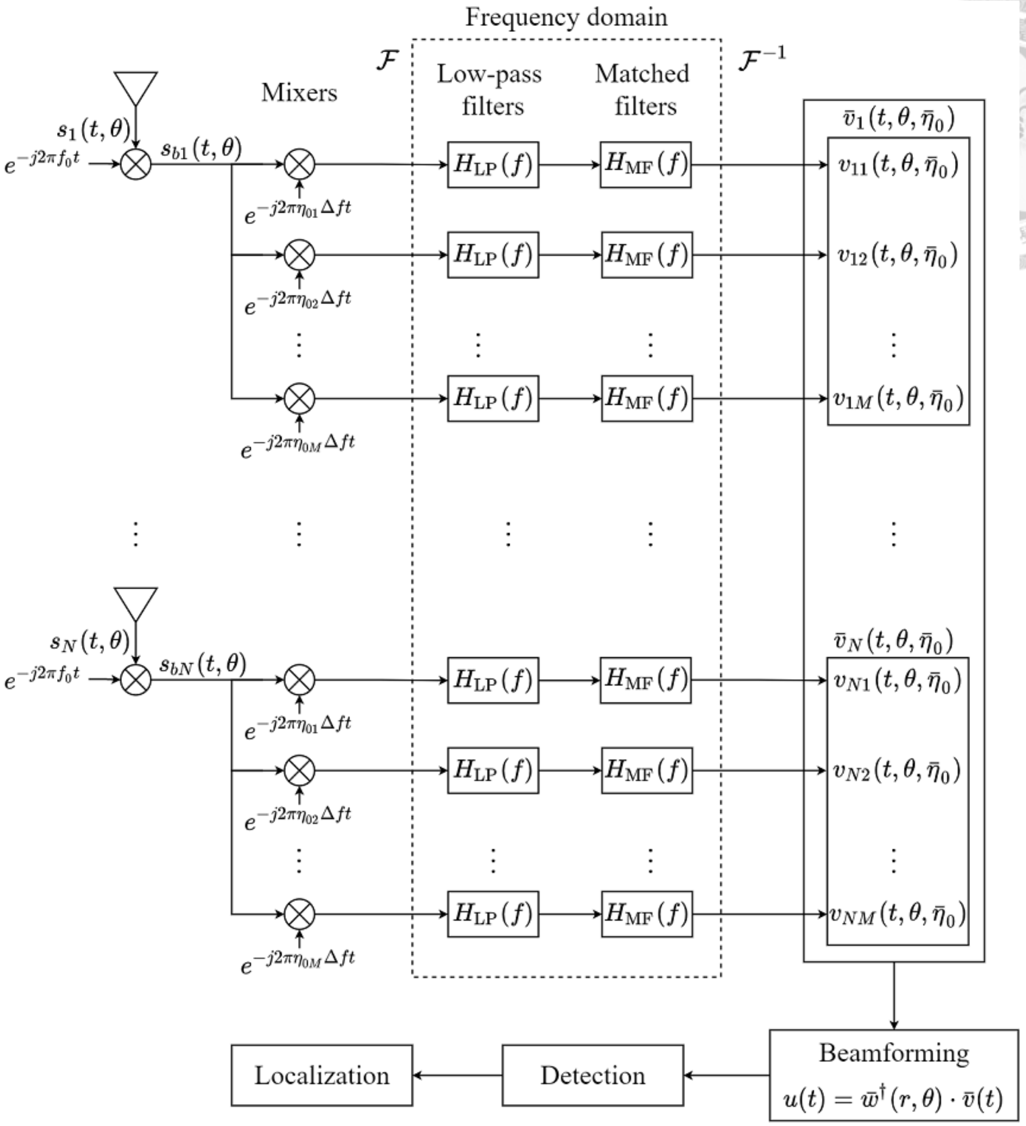

Figure 2.3: Schematic of receive array.

where the qth signal is

$$s_{qn}(t,\theta)=\sum_{m=1}^{M}\alpha_q w_{a\theta m} s_{tb}(t-\tau_{qmn})e^{j2\pi f_{qm}(t-\tau_{qmn})} \tag{2.8}$$

with $q=0$ for the target echo and $q=1,\cdots,Q$ for the jamming signals, where α_q and $f_{qm}=f_0+\eta_{qm}\Delta f$ are the amplitude and carrier frequency, respectively, of the qth signal.

The FD codes for the target echo and the qth jamming signal are $\bar{\eta}_0$ and $\bar{\eta}_q$, respectively, with $\bar{\eta}_0, \bar{\eta}_q \in \mathcal{C}$. The round-trip delay from the mth transmit-array element via the qth target to the nth receive-array element is

$$\tau_{qmn} = [2r_q - d_t(m-1)\sin\theta_q - d_r(n-1)\sin\theta_q]/c \tag{2.9}$$

where c is the speed of light. The true target is located at (r_0, θ_0), and the qth jamming signal is designed to camouflage a false-target at (r_q, θ_q). The Doppler frequency shift is neglected in this work. Assume that the total bandwidth of the received signal is much smaller than the carrier frequency, namely, $B + M_t\Delta f \ll f_0$, (2.8) can be approximated as

$$\hat{s}_{qn}(t,\theta) \simeq \sum_{m=1}^{M} \alpha_q w_{a\theta m} s_{tb}(t-\tau_q) e^{j2\pi(f_0+\eta_{qm}\Delta f)(t-\tau_q)} e^{jk_0 d_t(m-1)\sin\theta_q} e^{jk_0 d_r(n-1)\sin\theta_q}. \tag{2.10}$$

The round-trip delay of the target to the first element of both co-located arrays is $\tau_0 = 2r_0/c$. Assume the jamming signals are generated with a false-target generator (FTG) located at (r_j, θ_j), and the delay of the qth jammer is designed to be

$$\tau_q = \tau_j + \tau_{jq}, \quad q = 1, \cdots, Q \tag{2.11}$$

where $\tau_j = 2r_j/c$ is the time delay of the FTG to the first element of both co-located arrays, τ_{jq} is the camouflage delay controlled by the FTG, and $r_q = \tau_q c/2$.

The received signal in (2.7) is demodulated to the baseband as

$$s_{bn}(t,\theta) = s_n(t,\theta)e^{-j2\pi f_0 t} = s_{b0n}(t,\theta) + \sum_{q=1}^{Q} s_{bqn}(t,\theta) \tag{2.12}$$

doi:10.6342/NTU202302364

where $s_{bqn}(t,\theta) = s_{qn}(t,\theta)e^{-j2\pi f_0 t}$. The contribution in $s_{bqn}(t,\theta)$ from the mth transmit-array element is extracted by mixing $s_{bqn}(t,\theta)$ with a signal $e^{-j2\pi\eta_{0m}\Delta f t}$, followed by a low-pass filter $H_{\rm LP}(f) = {\rm rect}(f/B)$ and a matched filter $H_{\rm MF}(f) = S_{tb}^*(f)$, with the superscript $*$ denoting complex conjugate, to obtain

$$s_{bqnm}(t,\theta,\eta_{0m}) = \mathcal{F}^{-1}\left\{H_{\rm MF}(f)H_{\rm LP}(f)\mathcal{F}\left\{s_{bqn}(t,\theta)e^{-j2\pi\eta_{0m}\Delta f t}\right\}\right\} \tag{2.13}$$

where $\mathcal{F}$ and $\mathcal{F}^{-1}$ are Fourier transform and inverse Fourier transform, respectively, and

$$S_{tb}(f) = \mathcal{F}\{s_{tb}(t)\} = \int_{-\infty}^{\infty} s_{tb}(t)e^{-j2\pi f t}dt \tag{2.14}$$

is the Fourier transform of $s_{tb}(t)$. Thus, with the approximation in (2.10), (2.13) is reduced to

$$\begin{aligned} &s_{bqnm}(t,\theta,\eta_{0m}) = \\ &\qquad \alpha'_q e^{jk_0 d_r(n-1)\sin\theta_q} e^{-j2\eta_{0m}\Delta k r_q} \sum_{m'=1}^{M} w_{a\theta m'} h_{mm'}(t-\tau_q,\eta_{0m},\eta_{qm'}) e^{jk_0 d_t(m'-1)\sin\theta_q} \end{aligned} \tag{2.15}$$

where $\alpha'_q = \alpha_q e^{-j2\pi f_0 \tau_q}$, $\Delta k = 2\pi\Delta f/c$, and

$$\begin{aligned} h_{mm'}(t,\eta_{0m},\eta_{qm'}) &= \mathcal{F}^{-1}\left\{H_{mm'}(f,\eta_{0m},\eta_{qm'})\right\} \\ &= \mathcal{F}^{-1}\left\{S_{tb}^*(f){\rm rect}(f/B)S_{tb}(f-(\eta_{qm'}-\eta_{0m})\Delta f)\right\} \end{aligned} \tag{2.16}$$

is the code-matching response between elements m and m'.

All the signals $\{s_{bqnm}(t,\theta,\eta_{0m})\}$ in (2.15), with $q = 0, 1, \cdots, Q$, are stacked into an

doi:10.6342/NTU202302364

$MN \times 1$ vector

$$\bar{v}_q(t,\theta,\bar{\eta}_0) = [\bar{v}_{q1}^t(t,\theta,\bar{\eta}_0), \bar{v}_{q2}^t(t,\theta,\bar{\eta}_0), \cdots, \bar{v}_{qN}^t(t,\theta,\bar{\eta}_0)]^t \tag{2.17}$$

with

$$\bar{v}_{qn}(t,\theta,\bar{\eta}_0) = [s_{bqn1}(t,\theta,\eta_{01}), s_{bqn2}(t,\theta,\eta_{02}), \cdots, s_{bqnM}(t,\theta,\eta_{0M})]^t \tag{2.18}$$

Eqn.(2.17) is rewritten as $\bar{v}_q(t,\theta,\bar{\eta}_0) = \alpha_q' \bar{\mu}(r,\theta,\bar{\eta}_0; r_q,\theta_q,\bar{\eta}_q)$, with $r = ct/2$ and

$$\bar{\mu}(r,\theta,\bar{\eta}; r',\theta',\bar{\eta}') = \bar{b}(\theta') \otimes \bar{a}(r,\theta,\bar{\eta}; r',\theta',\bar{\eta}') \tag{2.19}$$

where $\otimes$ denotes Kronecker product, (r,θ) indicates the range-azimuth cell of interest, $\bar{\eta}$ is the FD code at the receive array, which matches the FD code of the transmit array to suppress jamming signal, namely, $\bar{\eta} = \bar{\eta}_0$, (r',θ') indicates the range-azimuth cell of a true target or a false-target jamming signal that carries FD code $\bar{\eta}' = \bar{\eta}_q$,

$$\bar{b}(\theta') = \left[1, e^{jk_0 d_r \sin\theta'}, \cdots, e^{jk_0 d_r (N-1)\sin\theta'}\right]^t \tag{2.20}$$

is the receive-azimuth steering vector, and

$$\bar{a}(r,\theta,\bar{\eta}; r',\theta',\bar{\eta}') = \bar{a}_r(r',\bar{\eta}) \odot \left\{\bar{\bar{h}}(t-\tau',\bar{\eta},\bar{\eta}') \cdot [\bar{w}_{a\theta}^*(\theta) \odot \bar{a}_\theta(\theta')]\right\} \tag{2.21}$$

is the transmit-array steering vector, $\odot$ denotes the Hadamard product, $\bar{a}_r(r',\bar{\eta})$ and $\bar{a}_\theta(\theta')$ are the transmit-range steering vector and transmit-azimuth steering vector, respectively,

doi:10.6342/NTU202302364

with the explicit forms of

$$\bar{a}_r(r', \bar{\eta}) = \left[e^{-j2\eta_1 \Delta k r'}, e^{-j2\eta_2 \Delta k r'}, \cdots, e^{-j2\eta_M \Delta k r'}\right]^t \tag{2.22}$$

$$\bar{a}_\theta(\theta') = \left[1, e^{jk_0 d_t \sin\theta'}, \cdots, e^{jk_0 d_t (M-1)\sin\theta'}\right]^t \tag{2.23}$$

$\bar{w}_{a\theta}(\theta)$ is the transmit-azimuth beamforming vector defined in (2.6), with $\bar{w}_{a\theta}(\theta) = \bar{a}_\theta(\theta)$ to point the beam to the azimuth θ of interest, and $\bar{\bar{h}}(t, \bar{\eta} = \bar{\eta}_0, \bar{\eta}' = \bar{\eta}_q)$ is an $M \times M$ code-matching matrix, with the mm'th element given in (2.16).

The received signals after demodulation can now be represented as

$$\bar{v}(t, \theta, \bar{\eta}_0) = \bar{v}_0(t, \theta, \bar{\eta}_0) + \sum_{q=1}^{Q} \bar{v}_q(t, \theta, \bar{\eta}_0) + \bar{z} \tag{2.24}$$

where $\bar{z} \sim \mathcal{CN}(\bar{0}_{MN}, \sigma_0^2 \bar{\bar{I}}_{MN\times MN})$ is a vector of zero-mean complex Gaussian noise, $\bar{0}_{MN}$ is a $MN \times 1$ zero vector, σ_0^2 is the variance of noise, and $\bar{\bar{I}}_{MN\times MN}$ is an $MN \times MN$ identity matrix.

Next, design a spotlight beamforming vector as

$$\bar{w}(r, \theta, \bar{\eta}_0) = \bar{w}_b(\theta) \otimes \bar{w}_{ar}(r, \bar{\eta}_0) \tag{2.25}$$

where $\bar{w}_b(\theta)$ is the spotlight-azimuth beamforming vector, which collaborates with $\bar{w}_{a\theta}(\theta)$ to form a beam in the azimuth direction θ of interest, leading to $\bar{w}_b(\theta) = \bar{b}(\theta)$, and $\bar{w}_{ar}(r, \bar{\eta}_0)$ is the spotlight-range beamforming vector for detecting targets in a range cell centered at r of

doi:10.6342/NTU202302364

interest, having the explicit form

$$\bar{w}_{ar}(r_s, \bar{\eta}_0) = [e^{j\phi_1}, e^{j\phi_2}, \cdots, e^{j\phi_M}]^t \tag{2.26}$$

where ϕ_m with $1 \leq m \leq M$ are implicitly dependent on the FD code $\bar{\eta}_0 \in \mathcal{C}$. The optimization of ϕ_m's will be elaborated in Section IV. The 2-norm of the spotlight beamforming vector $\bar{w}(r, \theta, \bar{\eta}_0)$ is MN.

The spotlight beamforming vector is then applied to $\bar{v}(t, \theta, \bar{\eta}_0)$ in (2.24) to obtain

$$u(t, \theta, \bar{\eta}_0) = \bar{w}^\dagger(r, \theta, \bar{\eta}_0) \cdot \bar{v}(t, \theta, \bar{\eta}_0) = u_0(t, \theta, \bar{\eta}_0) + \sum_{q=1}^{Q} u_q(t, \theta, \bar{\eta}_0) + n \tag{2.27}$$

where the superscript † denotes conjugate transpose,

$$u_q(t, \theta, \bar{\eta}_0) = \alpha'_q \bar{w}^\dagger(r, \theta, \bar{\eta}_0) \cdot \bar{\mu}(r, \theta, \bar{\eta}_0; r_q, \theta_q, \bar{\eta}_q) \tag{2.28}$$

$n = \bar{w}(r, \theta, \bar{\eta}_0) \cdot \bar{z}$, with $\sigma_n^2 = MN\sigma_0^2$. A spotlight response centered at (r, θ) is expected on $u(t, \theta, \bar{\eta}_0)$, with $r = ct/2$.

If the range, azimuth and FD code are matched at certain range-azimuth cell (r_s, θ_s), $\bar{w}^*_{a\theta}(\theta_s) \odot \bar{a}_\theta(\theta_s)$ in (2.21) is reduced to $\bar{I}_M$, the code-matching matrix is reduced to $\bar{\bar{h}}(0, \bar{\eta}_0, \bar{\eta}_0) = E\bar{\bar{I}}_{M\times M}$, hence the transmit-array beamforming vector in (2.21) is reduced to $E\bar{a}_r(r_s, \bar{\eta}_0)$. By choosing $\bar{w}(r_s, \theta_s, \bar{\eta}_0) = \bar{b}(\theta_s) \otimes \bar{a}_r(r_s, \theta_s)$, we have

$$\bar{w}^\dagger(r_s, \theta_s, \bar{\eta}_0) \cdot \bar{\mu}(r_s, \theta_s, \bar{\eta}_0; r_s, \theta_s, \bar{\eta}_0) = EMN \tag{2.29}$$

which implies a spotlight response centered at (r_s, θ_s).

Chapter 3

Design of FD Codebook

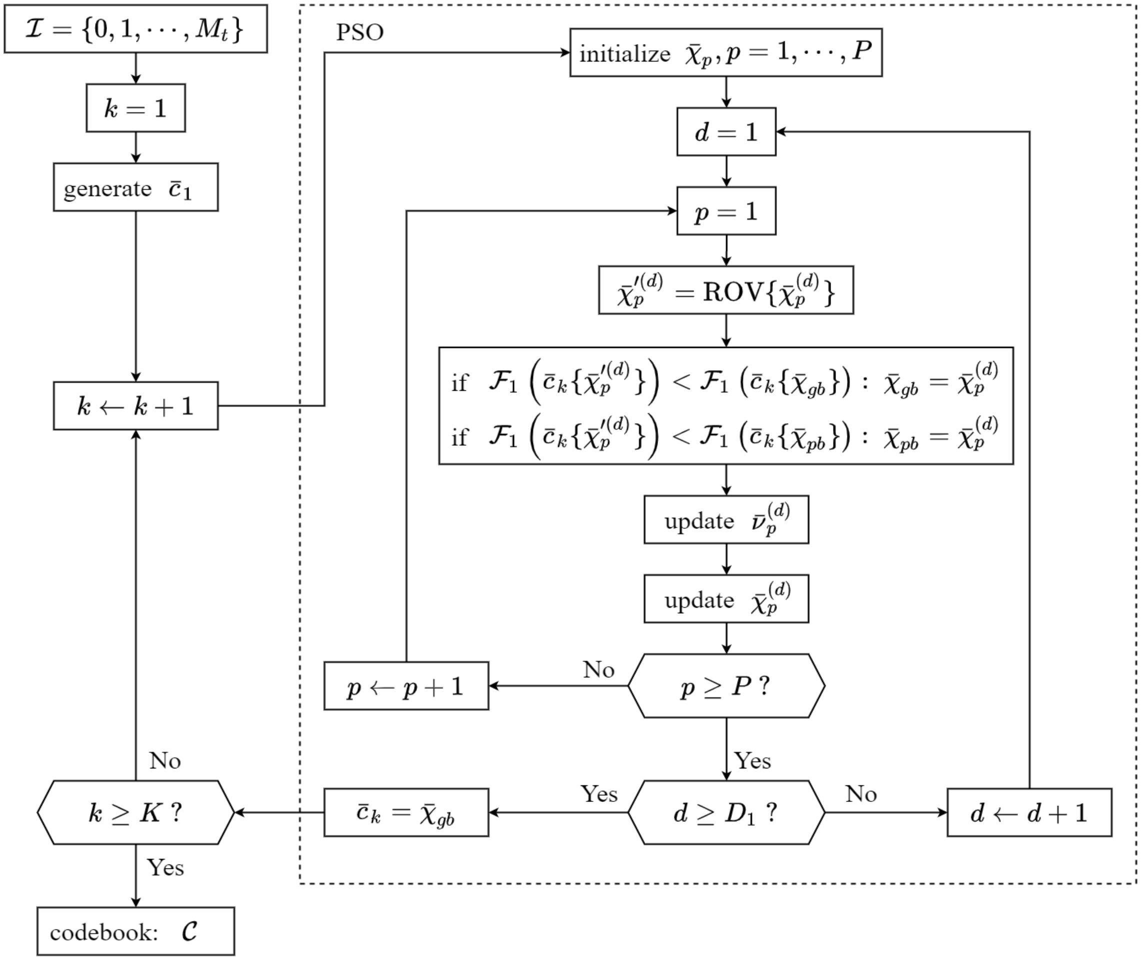

Figure 3.1: Flow-chart of selecting FD codes.

Jamming suppression is achieved by applying frequency-hopping scheme to induce mis-

doi:10.6342/NTU202302364

match between FD codes of target echo and jamming signals. Fig.3.1 shows the flow-chart of the proposed procedure of selecting FD codes in the codebook.

A total of K frequency-diverse (FD) codes are selected sequentially. The first FD code is generated by picking M candidates from the integer set $\mathcal{I} = \{0, 1, \cdots, M_t\}$. Each candidate is randomly picked with equal probability. If a newly picked candidate repeats with previous ones, it will be discarded and repicked. The M candidates serve as frequency offset indices (FOIs). They are arranged in an ascending order as $\bar{c}_1 = [c_{11}, c_{12}, \cdots, c_{1M}]^t$, with $c_{11} < c_{12} < \cdots < c_{1M}$ and $(c_{1M} - c_{11}) > 0.7M_t$. The condition $(c_{1M} - c_{11}) > 0.7M_t$ is imposed to acquire a sufficiently narrow half-power beamwidth (HPBW) of the spotlight response in the range domain. By analog, a uniform linear array with constant frequency increment across all the elements has an HPBW in range domain inversely proportional to the frequency difference between the first and the last elements.

Next, define the maximum jamming suppression level of the kth FD code $\bar{c}_k$ as

$$\mathcal{F}_1(\bar{c}_k) = \max_{1 \le k' \le k-1} J(\bar{c}_k, \bar{c}_{k'}) \tag{3.1}$$

where

$$J(\bar{c}_k, \bar{c}_{k'}) = -20 \log_{10} \frac{\|\bar{\bar{h}}(0, \bar{c}_k, \bar{c}_k)\|}{\|\bar{\bar{h}}(0, \bar{c}_k, \bar{c}_{k'})\|} \tag{3.2}$$

doi:10.6342/NTU202302364

is the jamming suppression level of $\bar{c}_k$ against previous FD code $\bar{c}_{k'}$, with

$$\|\bar{\bar{h}}(0, \bar{c}_k, \bar{c}_{k'})\| = \sqrt{\sum_{m=1}^{M} \sum_{m'=1}^{M} |h_{mm'}(0, c_{km}, c_{k'm'})|^2} \tag{3.3}$$

and

$$h_{mm'}(0, c_{km}, c_{k'm'}) = \int_{-\infty}^{\infty} S_{tb}^*(f)\mathrm{rect}(f/B)S_{tb}(f - (c_{k'm'} - c_{km})\Delta f)df \tag{3.4}$$

which is the integration between two overlapped spectra. When $c_{km} = c_{k'm'}$, (3.4) is reduced to

$$h_{mm}(0, c_{km}, c_{km}) = \int_{-B/2}^{B/2} |S_{tb}(f)|^2 df \tag{3.5}$$

The numerator and the denominator of (3.2) are proportional to the received energy if the FD code $\bar{c}_k$ matches and mismatches, respectively.

The kth FD code is selected among all $\bar{c}_k$'s that minimizes $\mathcal{F}_1(\bar{c}_k)$, namely,

$$\tilde{\bar{c}}_k = \arg\ \min_{\bar{c}_k} \mathcal{F}_1(\bar{c}_k) \tag{3.6}$$

A particle swarm optimization (PSO) algorithm with rank-order value (ROV) mapping [73] is applied to construct the FD codebook.

Define the position vector of the pth particle as

$$\bar{\chi}_p = [\chi_{p1}, \chi_{p2}, \cdots, \chi_{pM_t}]^t \tag{3.7}$$

where M_t is the maximum frequency offset index. Initially, each coordinate of $\bar{\chi}_p$ is a real number randomly picked from $[0,1]$. The ROV mapping converts a sequence of continuous variables to a permutation of integers. Each coordinate is mapped to the rank of its value, with the smallest coordinate mapped to 1, the next to 2, and so on. Explicitly, the pth particle is mapped to an ROV vector as $\bar{\chi}'_p = \mathrm{ROV}\{\bar{\chi}_p\}$. Since $\bar{\chi}'_p$ is a permutation of integer from 1 to M_t, the first M integers in $\bar{\chi}'_p$ are rearranged in ascending order to form an FD code, denoted by $\bar{c}_k\{\bar{\chi}'_p\}$. The fitness function is $\mathcal{F}_1(\bar{c}_k)$ in (3.1), and the order of the real-valued elements in $\bar{\chi}_p$ is adjusted to minimize $\mathcal{F}_1(\bar{c}_k)$.

The best fitness of the pth particle is labeled as *pbest*, associated with the best position vector $\bar{\chi}_{pb}$. The best fitness among the whole swarm is labeled as *gbest*, associated with the global best position vector $\bar{\chi}_{gb}$. The velocity of the pth particle is updated at iteration d as [74]

$$\bar{\nu}_p^{(d)} = h_w \bar{\nu}_p^{(d-1)} + \rho_1 \ \bar{\beta}_1 \odot (\bar{\chi}_{pb} - \bar{\chi}_p^{(d)}) + \rho_2 \ \bar{\beta}_2 \odot (\bar{\chi}_{gb} - \bar{\chi}_p^{(d)}) \tag{3.8}$$

where the components of $\bar{\beta}_1, \bar{\beta}_2$ are random real numbers from uniform distribution in $[0,1]$, $\bar{\chi}_p^{(d)}$ and $\bar{\nu}_p^{(d)}$ are the position vector and velocity vector, respectively, of particle p at iteration d. The habit weight h_w is linearly decreased from 0.9 to 0.4 with iterations, and $\rho_1 = \rho_2 = 2$ are empirical constants. The population size is set to $P = 20$ [40], and the velocity ceiling is set to $V_{\max} = 1$. The position of particle p is then updated as

$$\bar{\chi}_p^{(d+1)} = \bar{\chi}_p^{(d)} + \bar{\nu}_p^{(d)} \tag{3.9}$$

The PSO algorithm halts when the number of iterations reaches a pre-defined number D_1. The *gbest* at the end is mapped to an ROV vector as $\bar{\chi}'_{gb} = \mathrm{ROV}\{\bar{\chi}_{gb}\}$. The elements in $\bar{\chi}'_{gb}$ are rearranged in an ascending order to form an FD code $\bar{c}_k$.

doi:10.6342/NTU202302364

Chapter 4

Beamforming for Spotlight Response

The azimuth dependence of the spotlight response is controlled by the transmit-azimuth beamforming vector and the receive-azimuth beamforming vector. The range dependence of the spotlight response is achieved by orchestrating the frequency offsets across the transmit array with an FD code to form a transmit-range beamforming vector [32]-[40], as well as a spotlight-range beamforming vector, which will be optimized in this Section.

The spotlight response focused on a range-azimuth cell centered at (r_s, θ_s) is defined as

$$G_0(r, \theta) = G(r_s, \theta_s, \bar{\eta}_0; r, \theta, \bar{\eta}_0) \tag{4.1}$$

with

$$G(r_s, \theta_s, \bar{c}_k; r, \theta, \bar{c}_{k'}) = \left| \bar{w}^{\dagger}(r_s, \theta_s, \bar{c}_k) \cdot \bar{\mu}(r_s, \theta_s, \bar{c}_k; r, \theta, \bar{c}_{k'}) \right|^2 \tag{4.2}$$

where $\bar{\mu}(r_s, \theta_s, \bar{\eta}_0; r, \theta, \bar{\eta}_0)$ is defined in (2.19). The normalized spotlight response is defined as

$$g_0(r, \theta) = g(r_s, \theta_s, \bar{\eta}_0; r, \theta, \bar{\eta}_0) \tag{4.3}$$

doi:10.6342/NTU202302364

with

$$g(r_s, \theta_s, \bar{c}_k; r, \theta, \bar{c}_{k'}) = \frac{G(r_s, \theta_s, \bar{c}_k; r, \theta, \bar{c}_{k'})}{G(r_s, \theta_s, \bar{c}_k; r_s, \theta_s, \bar{c}_k)} \tag{4.4}$$

The spotlight response means a single peak centered in the specified range-azimuth cell and very low sidelobe level in the other cells.

The auto-correlation function of the LFM waveform significantly reduces the sidelobe level, which will be further reduced by optimizing the spotlight-range beamforming vector $\bar{w}_{ar}(r, \bar{\eta}_0)$. By substituting the spotlight beamforming vector in (2.25) into (4.1), we have

$$G_0(r, \theta) = G_{0b}(\theta) G_{0a}(r, \theta) \tag{4.5}$$

where

$$G_{0b}(\theta) = \left| \bar{w}_b^\dagger(\theta_s) \cdot \bar{b}(\theta) \right|^2 \tag{4.6}$$

$$G_{0a}(r, \theta) = \left| \bar{w}_{ar}^\dagger(r_s, \bar{\eta}_0) \cdot \bar{a}(r_s, \theta_s, \bar{\eta}_0; r, \theta, \bar{\eta}_0) \right|^2 \tag{4.7}$$

By choosing $\bar{w}_b(\theta_s) = \bar{b}(\theta_s)$, the azimuth response $G_b(\theta)$ is reduced to that of conventional MIMO arrays. In the response $G_{0a}(r, \theta)$, the transmit-azimuth beamforming vector $\bar{w}_{a\theta}(\theta)$ in (2.6) is used to optimize the azimuth response and $\bar{w}_{ar}(r_s, \bar{\eta}_0)$ in (2.26) is used to optimize the range response.

Fig.4.1 shows the flow-chart of optimizing the spotlight-range beamforming vector $\bar{w}_{ar}(r_s, \bar{\eta}_0)$

doi:10.6342/NTU202302364

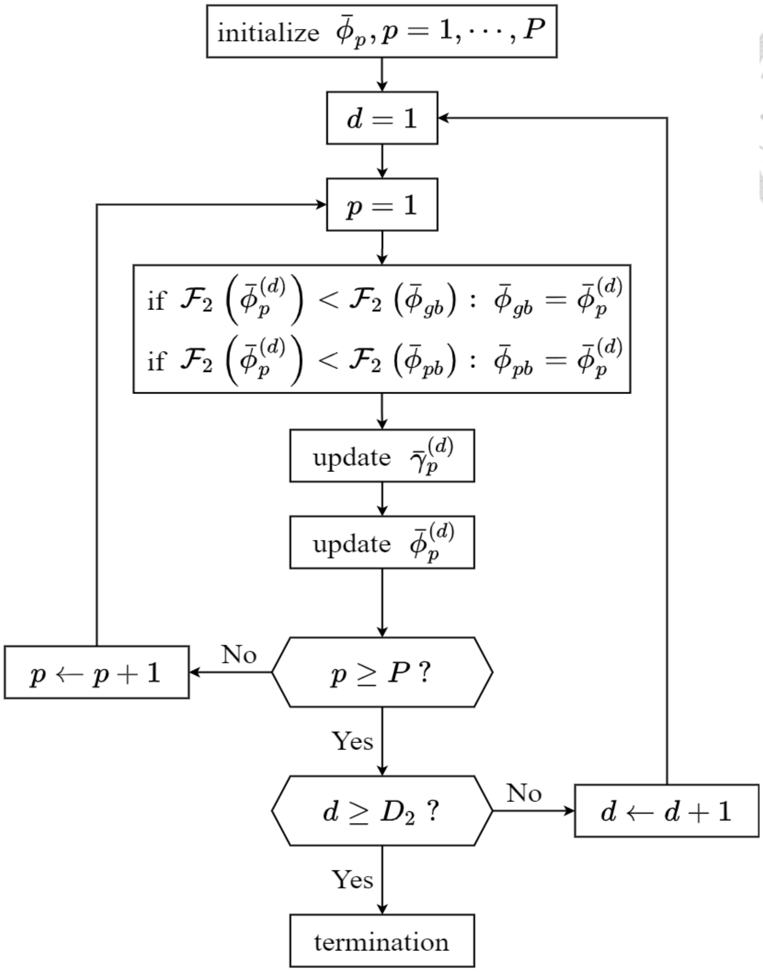

Figure 4.1: Flow-chart of optimizing spotlight-range beamforming vector.

in (2.26) with another PSO algorithm. Define the position vector $\bar{\phi}_p$ of the pth particle as

$$\bar{\phi}_p = [\phi_{p1}, \phi_{p2}, \cdots, \phi_{pM}]^t \tag{4.8}$$

with the initial value of ϕ_{pm} randomly picked from $[0, 2\pi]$.

Next, specify a normalized response mask $g_{\text{mask}}(r, \theta_s)$ as

$$10 \log_{10} g_{\text{mask}}(r, \theta_s) = \begin{cases} 0, & |r - r_s| \leq \Delta r/2 \\ -20, & \text{otherwise} \end{cases} \tag{4.9}$$

doi:10.6342/NTU202302364

and define a fitness function as

$$\mathcal{F}_2(\bar{\phi}_p) = \sum_{R_{\min} \le r \le R_{\max}} \max\left\{0, 10\log_{10} \frac{g_0(r, \theta_s; \bar{\phi}_p)}{g_{\text{mask}}(r, \theta_s)}\right\} \tag{4.10}$$

where $g_0(r, \theta_s; \bar{\phi}_p)$ is defined in (4.3), pending on $\bar{\phi}_p$, and the range cell of interest is $R_{\min} \le r \le R_{\max}$.

The best fitness of the pth particle is labeled as *pbest*, associated with the position vector $\bar{\phi}_{pb}$. The best fitness among the whole swarm is labeled as *gbest*, associated with the position vector $\bar{\phi}_{gb}$. The velocity of the pth particle is updated at iteration d as [74]

$$\bar{\gamma}_p^{(d)} = h_w \bar{\gamma}_p^{(d-1)} + \rho_1 \, \bar{\beta}_1 \odot (\bar{\phi}_{pb} - \bar{\phi}_p^{(d)}) + \rho_2 \, \bar{\beta}_2 \odot (\bar{\phi}_{gb} - \bar{\phi}_p^{(d)}) \tag{4.11}$$

where the components of $\bar{\beta}_1, \bar{\beta}_2$ are random real numbers from a uniform distribution in $[0, 1]$, $\bar{\phi}_p^{(d)}$ and $\bar{\gamma}_p^{(d)}$ are the position vector and velocity vector, respectively, of particle p at iteration d. The habit weight h_w is linearly decreased from 0.9 to 0.4 with iterations, and $\rho_1 = \rho_2 = 2$ are empirical constants. The population size is set to $P = 20$ [40], and the velocity ceiling $V_{\max}$ is set to 20 % that of the maximum position coordinate. The position of particle p is then updated as

$$\bar{\phi}_p^{(d+1)} = \bar{\phi}_p^{(d)} + \bar{\gamma}_p^{(d)} \tag{4.12}$$

The PSO algorithm halts when the number of iterations reaches a specified number D_2.

doi:10.6342/NTU202302364

The average normalized response to the target over all FD codes is computed as

$$g_t(r,\theta) = \frac{1}{K}\sum_{k=1}^{K} g(r_s,\theta_s,\bar{c}_k;r,\theta,\bar{c}_k) \tag{4.13}$$

and the average response to jamming signals is computed as

$$g_j(r,\theta) = \frac{1}{K(K-1)}\sum_{k=1}^{K}\sum_{k'\neq k} g(r_s,\theta_s,\bar{c}_k;r,\theta,\bar{c}_{k'}) \tag{4.14}$$

doi:10.6342/NTU202302364

Chapter 5

Target Detection and Localization

By applying the FH-LFM-FD-MIMO scheme to extract the signals that carry matched FD code and suppress the signals that carry mismatched FD codes, a target in a specific range-azimuth cell of size $\Delta r \times \Delta\theta$ can be detected at high signal-to-jamming-plus-noise ratio (SJNR).

The azimuth resolution of a conventional linear array is determined by the half-power beamwidth (HPBW) of the array as $0.88\lambda_0/(Md_t)$ radian [75], where Md_t is the aperture length of the linear array. The range resolution of the FH-LFM-FD-MIMO scheme is determined as

$$\Delta r = \min\left\{\frac{c}{2B}, \frac{c}{2M_t\Delta f}\right\} \tag{5.1}$$

The range resolution of conventional LFM radars is $\Delta r = c/(2B)$ [76], which is derived from the auto-correlation function of the LFM pulse

$$\begin{aligned}
&\left|h_{mm}(t,\eta_{0m},\eta_{0m})_{t=2r/c}\right| = \left|\mathcal{F}^{-1}\left\{S_{\text{tb}}(f)S^*_{\text{tb}}(f)\right\}\right| \\
&= \left|\int_{-\infty}^{\infty} s_{tb}(t')s^*_{tb}(t'-t)dt'\right| \\
&= E\left(1-\frac{|t|}{T}\right)\left|\text{sinc}\left[Bt\left(1-\frac{|t|}{T}\right)\right]\right|\text{rect}\left(\frac{r/c}{T}\right)
\end{aligned} \tag{5.2}$$

where sinc $(x) = \sin(\pi x)/(\pi x)$.

The array factor in the range domain of an FD-MIMO array operating with an FD code $\bar{\eta}$ is given by

$$|A_r(r,\bar{\eta})| = \left|\bar{w}^{\dagger}_{ar}(r_s,\bar{\eta})\cdot\bar{a}_r(r,\bar{\eta})\right| \tag{5.3}$$

To obtain a rough estimation of range resolution, consider uniform linear frequency increment Δf across the transmit-array elements and $\bar{w}_{ar}(r_s,\bar{\eta}) = [1,1,\cdots,1]^t$, the array factor is reduced to

$$|A_r(r,\bar{\eta})| = \left|\sum_{m=1}^{M} e^{-j2\pi(m-1)\Delta f(2r/c)}\right| = \left|\frac{\sin(2\pi M\Delta fr/c)}{\sin(2\pi\Delta fr/c)}\right| \tag{5.4}$$

which implies a range resolution of $\Delta r = c/(2M\Delta f)$ [77].

By analog, the HPBW in range domain is determined by the frequency span over the array, which is approximated as $(\eta_{\max}-\eta_{\min})\Delta f$, with $\eta_{\max}$ and $\eta_{\min}$ the maximum and minimum frequency-offset indices, respectively, within the FD code $\bar{\eta}$. The range response of the FH-LFM-FD-MIMO radar is jointly determined by the auto-correlation function of the LFM signals and the response of FD-MIMO array [77].

5.1 Target Detection

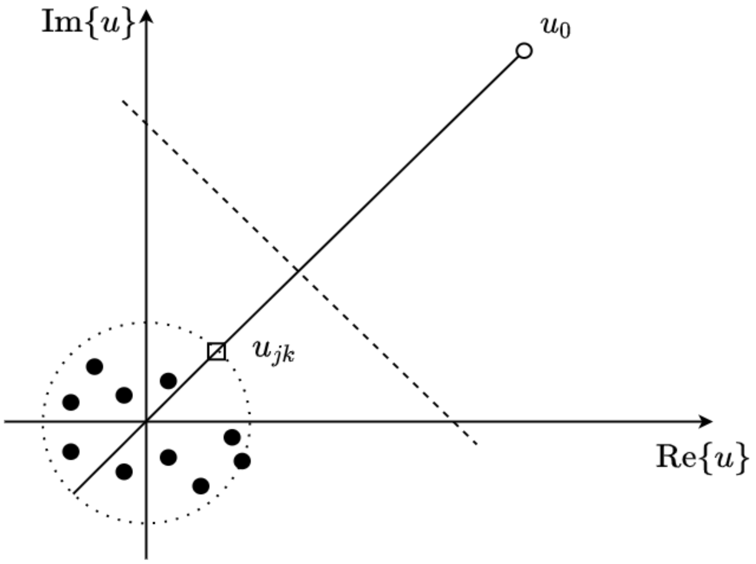

Figure 5.1: Target detection in u plane, ○: target echo, ●: jamming signals, □: strongest jamming signal, – – –: boundary line (threshold) when $\bar{\eta}_0 = \bar{c}_k \in \mathcal{C}$.

The signal after spotlight beamforming, $u_q(t, \theta, \bar{\eta}_0)$ in (2.28), is a complex number marked in Fig.5.1. The jamming signals after spotlight beamforming and FH jamming suppression tend to cluster around the origin of the complex plane, while the target echo, $u_0(t, \theta, \bar{\eta}_0)$, is deposited far away from the cluster. A boundary line (threshold) can be drawn for hypothesis test to separate jamming signals and the target echo. The strongest jamming signal u_{jk} is marked by $\otimes$. In a jamming-free environment, $u_{\mathrm{jk}} = 0$.

To detect targets at a specific range-azimuth cell centered at (r, θ), with azimuth res-

doi:10.6342/NTU202302364

olution $\Delta\theta$, range resolution Δr, and FD code $\bar{\eta}_0 = \bar{c}_k \in \mathcal{C}$, a binary hypothesis test is formulated as

$$\begin{cases} H_0: \quad u = u_{jk} + n \\ H_1: \quad u = u_0(t,\theta,\bar{\eta}_0) + n \end{cases} \tag{5.5}$$

where $t = 2r/c$, and

$$u_0(t,\theta,\bar{\eta}_0) = \alpha_0' \bar{w}^\dagger(r,\theta,\bar{\eta}_0) \cdot \bar{\mu}(r,\theta,\bar{\eta}_0; r,\theta,\bar{\eta}_0) \tag{5.6}$$

as in (2.28), with $q = 0$. The strongest jamming signal against $u_0(t,\theta,\bar{\eta}_0)$ has the magnitude of

$$|u_{jk}| = \max_{q=1,\cdots,Q} |\alpha_q' u_q(t,\theta,\bar{\eta}_0)| \tag{5.7}$$

and the same phase as u_0. Hypothesis H_0 holds if there is only noise in the specified range-azimuth cell.

Define the signal-to-noise ratio (SNR) at a single receive-array element as

$$\text{SNR} = \frac{E|\alpha_0|^2}{\sigma_0^2} \tag{5.8}$$

Without loss of generality, assume that the false-target jamming signals have the same strength as the true target echo. After FD code matching and spotlight beamforming, the signal-to-jamming-plus-noise ratio (SJNR) under the kth FD code is defined as

$$\text{SJNR}_k = \frac{|u_0|^2}{|u_{jk}|^2 + \sigma_n^2} \tag{5.9}$$

doi:10.6342/NTU202302364

where $\sigma_n^2 = MN\sigma_0^2$. The average SJNR over all the FD codes is computed as

$$\mathrm{SJNR} = \frac{1}{K}\sum_{k=1}^{K}\mathrm{SJNR}_k \tag{5.10}$$

The spotlight response also results in higher SJNR, improving the detection performance.

Previous FD methods [68], [71] located the false targets first and then synthesized a beampattern to suppress them in the spatial domain. Our approach suppresses the jamming signals by implementing a spotlight response with a distinctive FD code.

The binary test in (5.5) aims to decide if a target exists. Hypothesis H_0 holds if there is no target, while jamming and/or noise is present. Hypothesis H_1 holds if a target is present, possibly including jamming signals that carry matched FD code. Next, the boundary line between H_0 and H_1 in the u plane is determined by applying a log-likelihood ratio test (LLRT) as [78]

$$\ln\frac{p(u|H_1)}{p(u|H_0)} \underset{H_0}{\overset{H_1}{\gtrless}} \zeta_k \tag{5.11}$$

where $p(u|H_0)$ and $p(u|H_1)$ are the probability density function (PDF) of u when target is absent and present, respectively, and ζ_k is the threshold under $\bar{\eta}_0 = \bar{c}_k$. With the FH scheme, the threshold ζ_k depends on specific code $\bar{c}_k$ in the FD codebook, although the LLRT takes the same form as in conventional radar detection [78].

Eqn.(5.11) can be reduced to

$$\mathrm{Re}\{\psi_k\} \underset{H_0}{\overset{H_1}{\gtrless}} \eta_k \tag{5.12}$$

where

$$\psi_k = (u_0 - u_{jk})^* u \tag{5.13}$$

$$\eta_k = \frac{\sigma_n^2}{2}\zeta_k + \frac{|u_0|^2 - |u_{jk}|^2}{2} \tag{5.14}$$

Then, the false alarm rate is computed as

$$\begin{aligned} P_{fa} &= \mathrm{Prob}\left\{\ln\Lambda > \zeta_k | H_0\right\} = \mathrm{Prob}\left\{\mathrm{Re}\{\psi_k\} > \eta_k | H_0\right\} \\ &= \frac{1}{2}\left[1 - \mathrm{erf}\left(\frac{\eta_k - \mathrm{Re}\{(u_0 - u_{jk})^* u_{jk}\}}{\sqrt{(|u_0|^2 - |u_{jk}|^2)\sigma_n^2}}\right)\right] \end{aligned} \tag{5.15}$$

where erf(x) is the error function [78]. The threshold is determined, under a given P_{fa}, as

$$\eta_k = \mathrm{Re}\{(u_0 - u_{jk})^* u_{jk}\} + \sqrt{(|u_0|^2 - |u_{jk}|^2)\sigma_n^2}\ \mathrm{erf}^{-1}(1 - 2P_{fa}) \tag{5.16}$$

The probability of detection is then computed as

$$\begin{aligned} P_{dk} &= \mathrm{Prob}\left\{\ln\Lambda > \zeta_k | H_1\right\} = \mathrm{Prob}\left\{\mathrm{Re}\{\psi_k\} > \eta_k | H_1\right\} \\ &= \frac{1}{2}\left[1 - \mathrm{erf}\left(\frac{\eta_k - \mathrm{Re}\{(u_0 - u_{jk})^* u_0\}}{\sqrt{(|u_0|^2 - |u_{jk}|^2)\sigma_n^2}}\right)\right] \end{aligned} \tag{5.17}$$

Fig.5.2(a) shows the normalized threshold, $\eta_k/(|u_0|^2/\sigma_n^2)$, versus FD code index k, under false alarm rate of $P_{fa} = 10^{-2}$ and 10^{-4}, respectively, at SNR = 10 dB. The standard

doi:10.6342/NTU202302364

deviation of the normalized threshold is less than 15% of its average value, with either false alarm rate. Fig.5.2(b) shows the detection probability, P_{dk}, at SNR $= 0, -10, -15, -20$ dB, respectively, under $P_{fa} = 10^{-2}$.

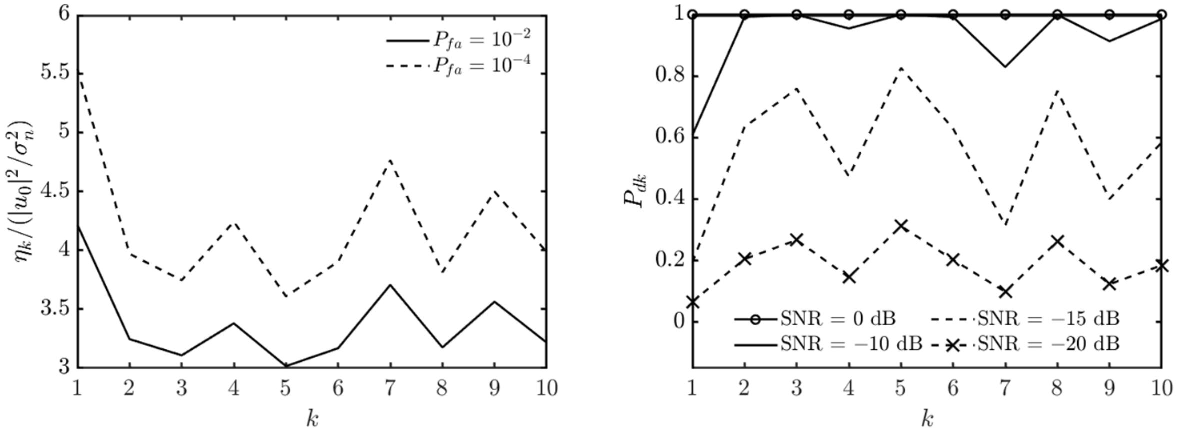

(a) (b)

Figure 5.2: (a) Normalized threshold, $\eta_k/(|u_0|^2/\sigma_n^2)$, versus FD code index k at different P_{fa}'s, SNR $= 10$ dB. (b) P_{dk} versus FD code index k, $P_{fa} = 10^{-2}$, at different SNRs.

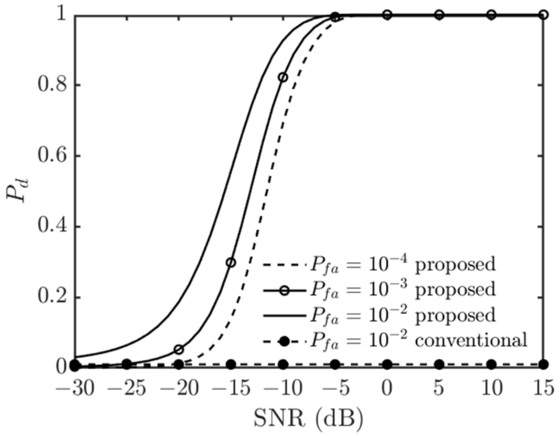

Figure 5.3: Average detection probability P_d versus SNR at different P_{fa}'s, conventional radar without FH scheme is shown for comparison.

doi:10.6342/NTU202302364

Fig.5.3 shows the average detection probability over all FD codes,

$$P_d = \frac{1}{K}\sum_{k=1}^{K} P_{dk} \tag{5.18}$$

versus SNR, under $P_{fa} = 10^{-2}, 10^{-3}$ and 10^{-4}, respectively. The detection probability of conventional radar without frequency-hopping (FH) scheme, under $P_{fa} = 10^{-2}$, is also shown for comparison. Without the FH scheme, the jamming signal may be mis-recognized as echo from a true target, namely, $u_{jam} = u_t$. Hence, the two PDFs $p(u|H_1)$ and $p(u|H_0)$ overlap with each other, making the detection probability equal to the false-alarm rate, regardless of SNR.

Fig.5.4(a) shows the SJNR versus FD code index k under various SNRs. As the SNR increases, the average SJNR increases, compatible with the increase of detection probability shown in Fig.5.2(b), which implies higher SJNR leading to higher detection probability. Fig.5.4(b) shows the average SJNR versus SNR. At SNR $= -5$ dB, the SJNR achieved with the proposed approach is 15 dB, which is sufficiently high to make the detection probability close to 1, under $P_{fa} = 10^{-2}, 10^{-3}, 10^{-4}$, respectively, as shown in Fig.5.3.

The SJNR of conventional method saturates at 0 dB, as we assume the jamming signals can be comparable to the signal amplitude of the true target. On the other hand, the SJNR of the proposed approach is higher than 20 dB at high SNR. This level of improvement will be verified later in Fig.6.3(b) where the jamming signals at the center of the spotlight

doi:10.6342/NTU202302364

response are suppressed by more than 20 dB.

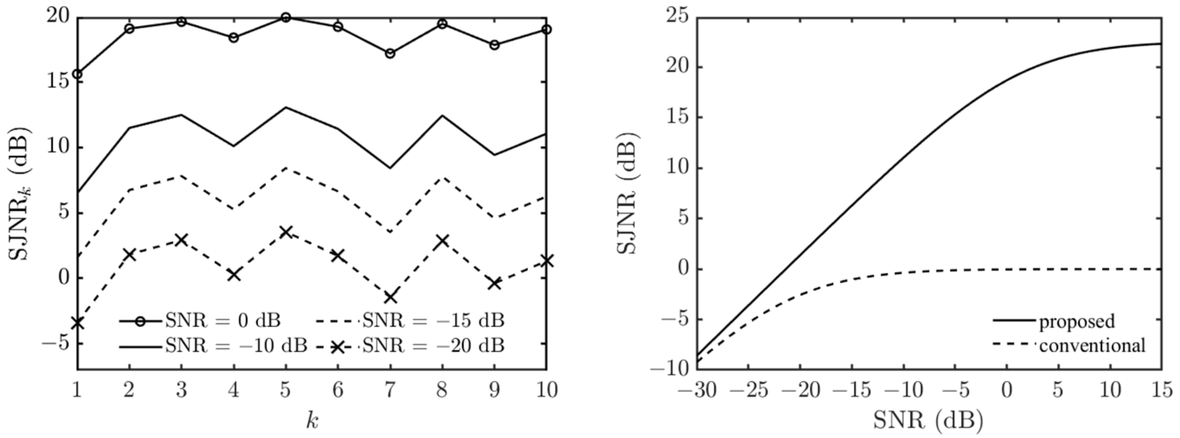

(a) (b)

Figure 5.4: (a) SJNR versus FD code index k at different SNRs. (b) Average SJNR versus SNR.

The false-alarm rate P_{fa} in (5.15) is derived in one PRI, under the condition that the jamming signals and the target echo carry different FD codes. However, the FTG may happen to match the FD code of the transmit-array with probability p_g. Hence, the false alarm rate and the detection probability are corrected as P'_{fa} and P'_d, respectively, with

$$P'_{fa} = P_{fa} + p_g P_d \tag{5.19}$$

$$P'_d = (1 - p_g) P_d \tag{5.20}$$

where the false-alarm rate induced by the jamming signal with mismatched FD code is P_{fa}, and that induced by the jamming signal with matched FD code is $p_g P_d$. The probability of detecting a true target is modified by excluding the probability of detecting the jamming signal with matched FD code from P_d.

The probability p_g depends on the design of FH sequence $\mathcal{S}$ and the strategy adopted by the FTG. If the FTG randomly selects an FD code among the K FD codes, we have $p_g = 1/K$, which is typically much larger than P_{fa}, leading to $p_g P_d \gg P_{fa}$ in (5.19).

By implementing a frequency-hopping scheme, different FD codes are applied in different PRIs. It is possible that the FTG may accidentally match the FD code in some PRIs and induce strong jamming signal into the range-azimuth cell of interest. To increase the overall detection probability, binary hypothesis tests in (5.12) are conducted in L PRIs, with different FD codes orchestrated in different PRIs. A target is claimed if the H_1 hypothesis holds at least L_1 out of L tests. The overall detection probability is thus computed as

$$P_{dL} = \sum_{\ell=L_1}^{L} \binom{L}{\ell} (P_d')^{\ell} (1 - P_d')^{L-\ell} \tag{5.21}$$

Similarly, the overall false alarm rate is computed as

$$P_{faL} = \sum_{\ell=L_1}^{L} \binom{L}{\ell} (P_{fa}')^{\ell} (1 - P_{fa}')^{L-\ell} \tag{5.22}$$

Fig.5.5 shows the effect of L and L_1 on P_{dL} and P_{faL}, respectively. Fig.5.5(c) indicates that high value of $P_{dL} = 0.995$ and fairly low value of $P_{faL} = 7 \times 10^{-4}$ can be achieved by choosing $L = 8$ and $L_1 = 5$.

Fig.5.6 shows the values of P_{dL} and P_{faL}, with $L_1 = L/2 + 1$ and $p_g = 0.05$, where p_g is one half of its counterpart in Fig.5.5(c). It is observed that $P_{dL} = 0.998$ and $P_{faL} = 2 \times 10^{-4}$

doi:10.6342/NTU202302364

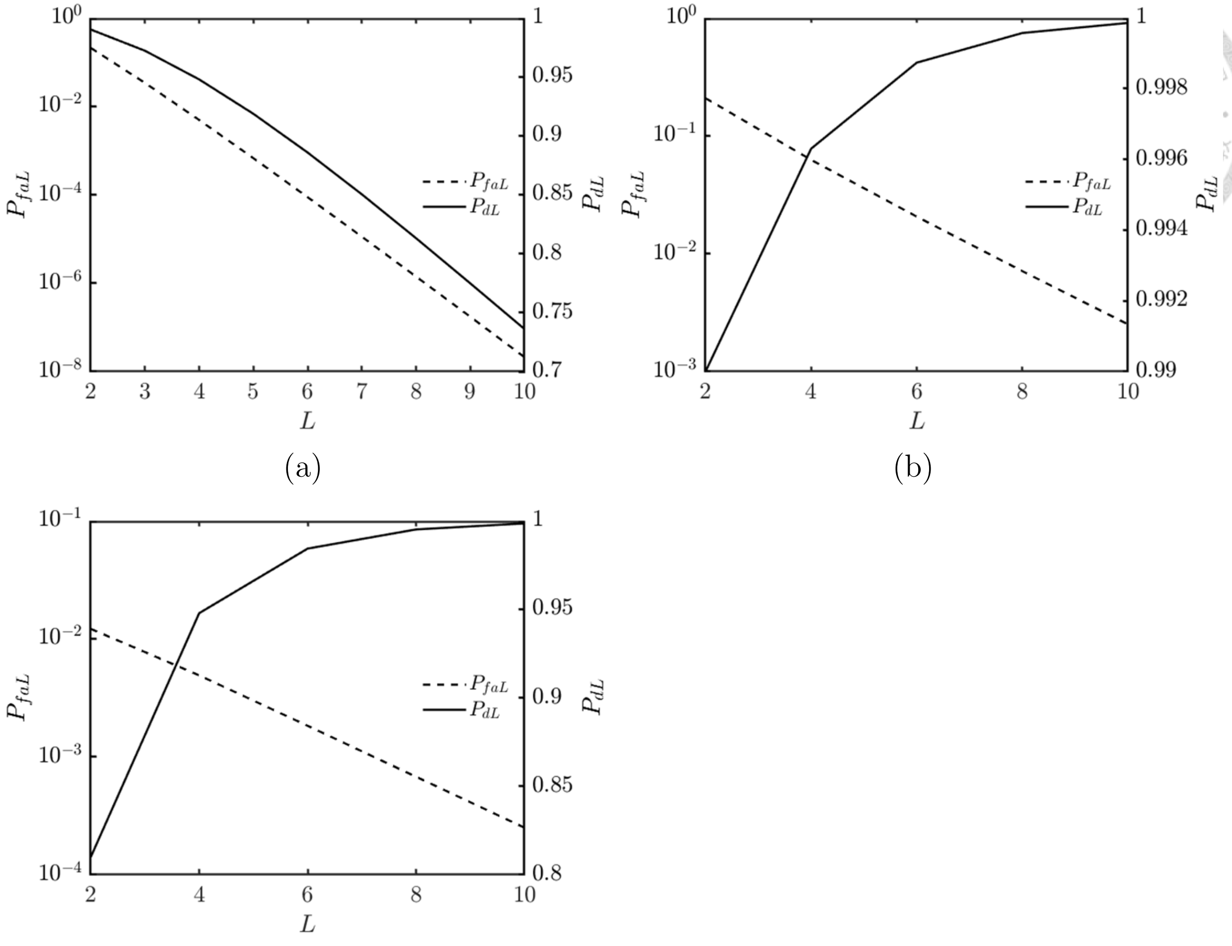

(a)

(b)

(c)

Figure 5.5: Effect of L and L_1 on P_{dL} and P_{faL}, (a) $L_1 = L - 1$, (b) $L_1 = L/2$, (c) $L_1 = L/2 + 1$, $P_{fa} = 10^{-2}$, $p_g = 0.1$, SNR = 10 dB.

are achieved by choosing $L = 6$ and $L_1 = 4$, which implies higher detection probability and lower false alarm rate can be achieved within fewer PRIs if p_g is smaller.

5.2 Target Localization

By applying the target detection scheme, a target is claimed in the range-azimuth cell centered at $(\tilde{r}_0, \tilde{\theta}_0)$, denoted as $\Gamma = \{|r - \tilde{r}_0| \leq \Delta r/2, |\theta - \tilde{\theta}_0| \leq \Delta\theta/2\}$. The precision of the target location can be further improved by applying a two-dimensional MVDR spectrum

doi:10.6342/NTU202302364

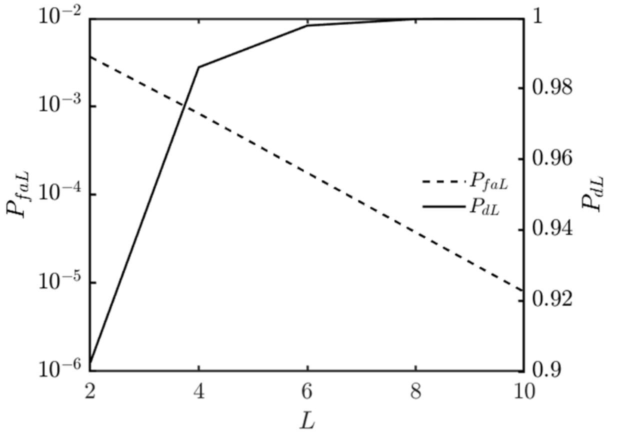

Figure 5.6: Values of P_{dL} and P_{faL} with $L_1 = L/2+1$, $P_{fa} = 10^{-2}$, $p_g = 0.05$, SNR = 10 dB.

[65]. With the spotlight response of the FH-LFM-FD-MIMO array, the two-dimensional MVDR spectrum can be computed only within the specific range-azimuth cell to pinpoint the target, significantly saving the computational time.

To begin with, compute the correlation matrix of the received signals over L PRIs as

$$\bar{\bar{\Omega}} = \mathrm{E}\left\{\bar{v}(\tilde{\tau}_0,\tilde{\theta}_0,\bar{\eta}_0)\bar{v}^\dagger(\tilde{\tau}_0,\tilde{\theta}_0,\bar{\eta}_0)\right\} = \frac{1}{L}\sum_{\ell=1}^{L}\bar{v}(\tilde{\tau}_0,\tilde{\theta}_0,\bar{\eta}_0^{(\ell)})\bar{v}^\dagger(\tilde{\tau}_0,\tilde{\theta}_0,\bar{\eta}_0^{(\ell)}) \tag{5.23}$$

where $\bar{\eta}_0^{(\ell)}$ is the FD code assigned in the ℓth PRI, based on the FH sequence $\mathcal{S}$. Then, the MVDR spectrum is computed as [65]

$$\begin{aligned} P(r,\theta) = \bar{w}_{\mathrm{mvdr}}^\dagger \cdot \bar{\bar{\Omega}} \cdot \bar{w}_{\mathrm{mvdr}} = \Big\{ & \bar{\mu}^\dagger(\tilde{r}_0,\tilde{\theta}_0,\bar{\eta}_0;r,\theta,\bar{\eta}_0) \\ & \cdot\bar{\bar{\Omega}}^{-1}\cdot\bar{\mu}(\tilde{r}_0,\tilde{\theta}_0,\bar{\eta}_0;r,\theta,\bar{\eta}_0)\Big\}^{-1}, \quad (r,\theta)\in\Gamma \end{aligned} \tag{5.24}$$

where $\bar{w}_{\text{mvdr}}$ is the optimal solution of the following optimization problem [79]

$$\bar{w}_{\text{mvdr}} = \arg\ \min_{\bar{w}}\ \left\{\bar{w}^\dagger \cdot \bar{\bar{\Omega}} \cdot \bar{w}\right\}$$

$$\text{s.t. } \bar{w}^\dagger \cdot \bar{\mu}(\tilde{r}_0, \tilde{\theta}_0, \bar{\eta}_0; r, \theta, \bar{\eta}_0) = 1 \tag{5.25}$$

which has the explicit form

$$\bar{w}_{\text{mvdr}} = \left\{\bar{\mu}^\dagger(\tilde{r}_0, \tilde{\theta}_0, \bar{\eta}_0; r, \theta, \bar{\eta}_0) \cdot \bar{\bar{\Omega}}^{-1}\right.$$

$$\left. \cdot \bar{\mu}(\tilde{r}_0, \tilde{\theta}_0, \bar{\eta}_0; r, \theta, \bar{\eta}_0)\right\}^{-1} \left\{\bar{\bar{\Omega}}^{-1} \cdot \bar{\mu}(\tilde{r}_0, \tilde{\theta}_0, \bar{\eta}_0; r, \theta, \bar{\eta}_0)\right\} \tag{5.26}$$

Note that the MVDR spectrum will indicate the position of the true target only when the FD code in (2.19) is matched, namely, $\bar{\eta} = \bar{\eta}' = \bar{\eta}_0$. As $\bar{\eta}_0$ in the present PRI is recorded in $\mathcal{S}$, it can be used to compute $\bar{\mu}(\tilde{r}_0, \tilde{\theta}_0, \bar{\eta}_0; r, \theta, \bar{\eta}_0)$, then $P(r, \theta)$ in (5.24). Finally, the precise target location is estimated as

$$(\hat{r}_0, \hat{\theta}_0) = \arg\ \max_{(r,\theta)}\ P(r, \theta) \tag{5.27}$$

The precision of the target location is limited by the Cramér-Rao bound (CRB) [53], which is the minimum variance an unbiased estimator can achieve. Let $\bar{\xi} = [r_0, \theta_0]^t$, the Fisher information matrix (FIM) for $\bar{\xi}$ is [55]

$$\bar{\bar{\Xi}} = 2|\alpha_0|^2 \text{Re}\left\{\bar{\bar{D}}^\dagger \cdot \bar{\bar{\Omega}}^{-1} \cdot \bar{\bar{D}}\right\} \tag{5.28}$$

where

$$\bar{\bar{D}} = \frac{\partial \bar{\mu}(r, \theta, \bar{\eta}_0)}{\partial \bar{\xi}} = [\bar{D}_r, \bar{D}_\theta] \tag{5.29}$$

is an $MN \times 2$ matrix, with

$$\bar{D}_r = \frac{\partial \bar{\mu}(r, \theta, \bar{\eta}_0)}{\partial r} = \bar{b}(\theta) \otimes \frac{\partial \bar{a}(\tilde{r}_0, \tilde{\theta}_0, \bar{\eta}_0; r, \theta, \bar{\eta}_0)}{\partial r} \tag{5.30}$$

$$\bar{D}_\theta = \frac{\partial \bar{\mu}(r, \theta, \bar{\eta}_0)}{\partial \theta} = \frac{\partial \bar{b}(\theta)}{\partial \theta} \otimes \bar{a}(\tilde{r}_0, \tilde{\theta}_0, \bar{\eta}_0; r, \theta, \bar{\eta}_0) + \bar{b}(\theta) \otimes \frac{\partial \bar{a}(\tilde{r}_0, \tilde{\theta}_0, \bar{\eta}_0; r, \theta, \bar{\eta}_0)}{\partial \theta} \tag{5.31}$$

By using (2.19), (2.20) and (2.21), the elements of $\bar{D}_r$ and $\bar{D}_\theta$ are derived as

$$\frac{\partial \bar{b}(\theta)}{\partial \theta} = jk_0 d_r \cos\theta \ \mathrm{diag}\{0, 1, \cdots, N-1\} \cdot \bar{b}(\theta) \tag{5.32}$$

$$\frac{\partial \bar{a}(\tilde{r}_0, \tilde{\theta}_0, \bar{\eta}_0; r, \theta, \bar{\eta}_0)}{\partial r} = -j2\Delta k \ \mathrm{diag}\{\bar{\eta}_0\} \cdot \bar{a}(\tilde{r}_0, \tilde{\theta}_0, \bar{\eta}_0; r, \theta, \bar{\eta}_0) \tag{5.33}$$

$$\begin{aligned} \frac{\partial \bar{a}(\tilde{r}_0, \tilde{\theta}_0, \bar{\eta}_0; r, \theta, \bar{\eta}_0)}{\partial \theta} &= \bar{a}_r(r, \bar{\eta}_0) \odot \Big[\bar{\bar{h}}(2(r - \tilde{r}_0)/c, \bar{\eta}_0, \bar{\eta}_0) \\ &\cdot jk_0 d_t \cos\theta \ \mathrm{diag}\{0, 1, \cdots, M-1\} \cdot \Big(\bar{w}^*_{a\theta}(\tilde{\theta}_0) \odot \bar{a}_\theta(\theta) \Big) \Big] \end{aligned} \tag{5.34}$$

where diag$\{\bar{\eta}_0\}$ means a diagonal matrix with elements of $\bar{\eta}_0$ on the diagonal. The FIM is thus reduced to

$$\bar{\bar{\Xi}} = 2|\alpha_0|^2 \begin{bmatrix} \bar{D}_r^\dagger \cdot \bar{\bar{\Omega}}^{-1} \cdot \bar{D}_r & \mathrm{Re}\{\bar{D}_r^\dagger \cdot \bar{\bar{\Omega}}^{-1} \cdot \bar{D}_\theta\} \\ \mathrm{Re}\{\bar{D}_r^\dagger \cdot \bar{\bar{\Omega}}^{-1} \cdot \bar{D}_\theta\} & \bar{D}_\theta^\dagger \cdot \bar{\bar{\Omega}}^{-1} \cdot \bar{D}_\theta \end{bmatrix} \tag{5.35}$$

The CRBs on range and azimuth, denoted as $(\delta r)^2$ and $(\delta\theta)^2$, respectively, are the diagonal

doi:10.6342/NTU202302364

elements of the inverse of FIM, namely,

$$(\delta r)^2 = \frac{\bar{D}_\theta^\dagger \cdot \bar{\bar{\Omega}}^{-1} \cdot \bar{D}_\theta}{2|\alpha_0|^2 \det \left\{ \mathrm{Re} \left\{ \bar{\bar{D}}^\dagger \cdot \bar{\bar{\Omega}}^{-1} \cdot \bar{\bar{D}} \right\} \right\}} \tag{5.36}$$

$$(\delta \theta)^2 = \frac{\bar{D}_r^\dagger \cdot \bar{\bar{\Omega}}^{-1} \cdot \bar{D}_r}{2|\alpha_0|^2 \det \left\{ \mathrm{Re} \left\{ \bar{\bar{D}}^\dagger \cdot \bar{\bar{\Omega}}^{-1} \cdot \bar{\bar{D}} \right\} \right\}} \tag{5.37}$$

In jamming-free environment, the covariance matrix in (5.23) is reduced to $\bar{\bar{\Omega}} = \sigma_0^2 \bar{\bar{I}}_{MN}$, then (5.36) and (5.37) are reduced to

$$(\delta r)^2 = \frac{\sigma_0^2}{2|\alpha_0|^2} \frac{|\bar{D}_\theta|^2}{\det \left\{ \mathrm{Re} \left\{ \bar{\bar{D}}^\dagger \cdot \bar{\bar{D}} \right\} \right\}} \tag{5.38}$$

$$(\delta \theta)^2 = \frac{\sigma_0^2}{2|\alpha_0|^2} \frac{|\bar{D}_r|^2}{\det \left\{ \mathrm{Re} \left\{ \bar{\bar{D}}^\dagger \cdot \bar{\bar{D}} \right\} \right\}} \tag{5.39}$$

which become smaller (higher precision) by increasing the SNR.

The range resolution Δr and the azimuth resolution $\Delta\theta$ are determined by the HPBWs of the response function in range and azimuth, respectively, which depend on the physical configurations of the transmit-array and the receive-array. It does not take full advantage of the information embedded in the received signals.

The two-dimensional MVDR spectrum exploits the covariance matrix of the received signals to enhance the estimation precision from $(\Delta r, \Delta\theta)$ to $(\delta r, \delta\theta)$. A target is first detected within a range-azimuth cell of size $\Delta r \times \Delta\theta$, then the MVDR spectrum is computed to search for the fine target location, achieving precisions on the order of $(\delta r, \delta\theta)$. The computational cost is significantly reduced by carrying out fine search only in the range-azimuth cell of interest.

doi:10.6342/NTU202302364

Chapter 6

Simulations and Discussions

Table 6.1: Parameters used in simulations.

parameter	symbol	value
reference frequency	f_0	10 GHz [43]
waveform bandwidth	B	1 MHz [44]
waveform duration	T	100 μs [81]
number of transmit-array elements	M	17 [36],[40]
number of receive-array elements	N	17
maximum frequency modulation index	M_t	500
frequency step	Δf	10 kHz
pulse repetition interval	PRI	1 ms [80]
number of FD codes	K	10

Table 6.1 lists the parameters used in the simulations. The reference frequency and the waveform bandwidth are 10 GHz and 1 MHz, respectively [43], [44]. The maximum range is 150 km at the pulse repetition interval of 1 ms, without causing range ambiguity [80]. The waveform duration is $T = 100\mu$s [81]. The number of elements in both transmit and receive arrays is 17 [36], [40]. The number of FD codes is $K = 10$. Based on the parameters listed in Table 6.1, we have $\Delta r = c/(2M_t\Delta f) = 30$ m and $\Delta\theta = 0.88\lambda_0/(Md_t)$ (rad)$= 5.9^\circ$.

Fig.6.1 shows an optimal codebook of $K = 10$, designed with the method in Section III.

doi:10.6342/NTU202302364

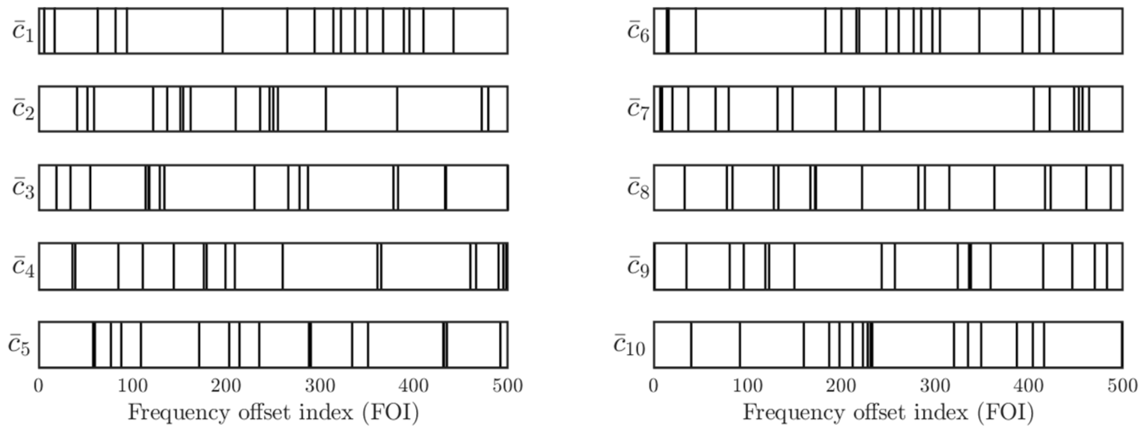

(a) (b)

Figure 6.1: An optimal FD codebook of $K = 10$, (a) $\bar{c}_1 \sim \bar{c}_5$, (b) $\bar{c}_6 \sim \bar{c}_{10}$.

The vertical lines in each FD code mark the chosen frequency offset indices. Table 6.2 lists the jamming suppression levels between different FD codes, where the value of $-J(\bar{c}_k, \bar{c}_{k'})$ in (3.2) is listed in the kth row and the k'th column. All the diagonal elements are equal to 0 dB and all the off-diagonal elements are larger than 30 dB, indicating that signals emitted under different FD codes will be suppressed by more than 30 dB with the proposed approach.

Table 6.2: Jamming suppression levels between different FD codes.

$k \backslash k'$	1	2	3	4	5	6	7	8	9	10
1	0.0	32.1	31.3	31.4	31.5	30.8	31.2	31.5	31.4	31.0
2	33.3	0.0	30.9	32.2	31.2	32.0	31.5	31.1	31.1	31.4
3	32.3	32.3	0.0	31.1	31.5	31.5	31.0	31.5	31.5	31.8
4	32.0	32.1	32.2	0.0	30.8	32.5	31.8	31.2	30.9	30.9
5	31.6	31.4	31.7	31.5	0.0	31.5	31.8	31.2	30.9	30.9
6	31.4	31.4	31.3	31.6	31.9	0.0	31.4	31.3	31.8	31.3
7	31.2	31.3	31.4	31.5	31.5	31.2	0.0	31.3	31.8	31.6
8	31.6	31.3	31.5	31.6	31.4	31.4	31.5	0.0	31.1	31.4
9	31.2	31.4	31.4	31.1	31.6	32.2	31.3	31.9	0.0	31.2
10	31.4	31.5	31.2	31.8	32.1	32.1	31.2	32.0	31.7	0.0

Fig.6.2 shows the average normalized response in (4.13) and the average response to

doi:10.6342/NTU202302364

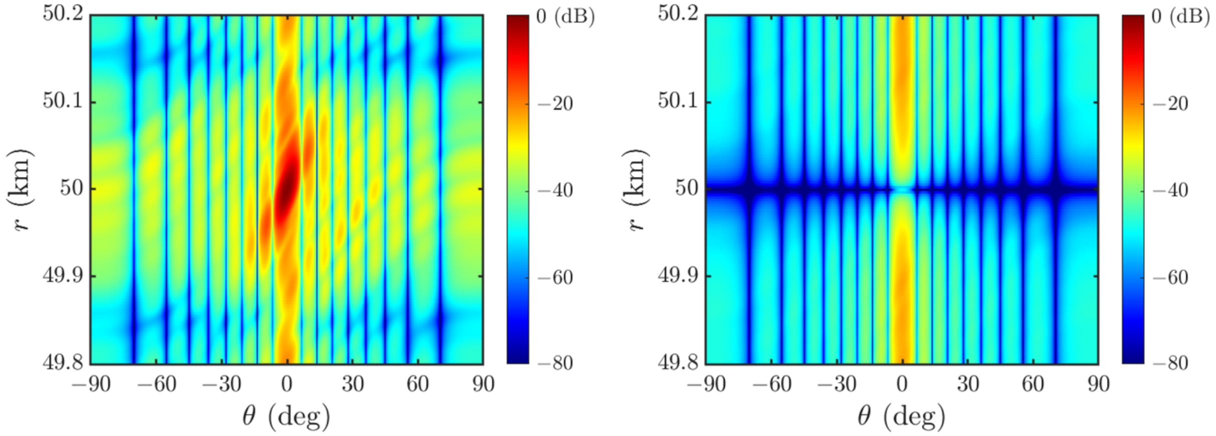

(a)

(b)

Figure 6.2: Range-azimuth profiles of (a) average normalized response defined in (4.13) and (b) average response to jamming signals defined in (4.14).

jamming signals in (4.14). The center of the spotlight is chosen as $(r_s, \theta_s) = (50\ \text{km}, 0°)$. Fig.6.2(a) shows a single peak at the center, with HPBW of 30 m in range and 6° in azimuth. The first sidelobe is about −20 dB. Fig.6.2(b) shows the average response to jamming signals, of which the maximum is −21.7 dB.

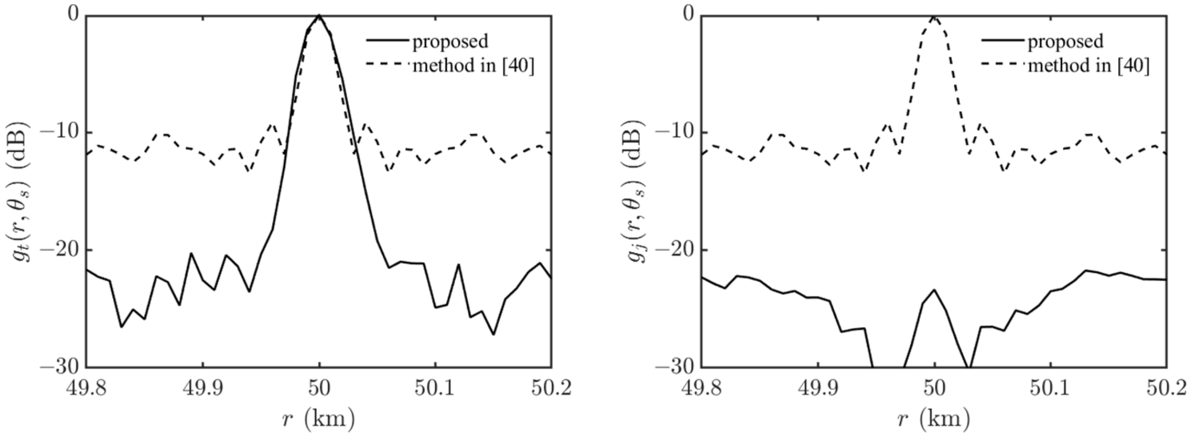

(a)

(b)

Figure 6.3: Range profiles of (a) average normalized response defined in (4.13) and (b) average response to jamming signals defined in (4.14), at $\theta_s = 0°$.

doi:10.6342/NTU202302364

Fig.6.3 shows the range profiles of average normalized response in (4.13) and average response to jamming signals in (4.14), respectively, at $\theta_s = 0°$. The responses in [40] is also shown for comparison. Fig.6.3(a) shows that the proposed approach achieves the mainlobe width of 30 m, comparable to that in [40], while significantly reducing the sidelobe level from about -10 dB in [40] to lower than -20 dB.

Fig.6.3(b) shows that the jamming response is significantly suppressed by more than 20 dB with the proposed approach. In comparison, the jamming response with conventional approach is indistinguishable from the target response shown in Fig.6.3(a).

Fig.6.4 shows the two-dimensional MVDR spectrum in the target range-azimuth cell centered at $\theta_s = 0°$ and $r_s = 50$ km, as well as two profiles of spectrum at $\theta_s = 0°$ and $r_s = 50$ km, respectively. The target is pinpointed to a small area of $\delta r \times \delta\theta$, much smaller than $\Delta r \times \Delta\theta$.

Fig.6.5 shows the ratios of $\delta r/\Delta r$ and $\delta\theta/\Delta\theta$, respectively, versus SNR. Both ratios depend linearly on the inverse of SNR, consistent with (5.38) and (5.39). Note that the range resolution Δr and the azimuth resolution $\Delta\theta$ are determined by the length of antenna arrays and the FD code.

Fig.6.5(a) shows that $\delta\theta$ is about 40 times smaller than $\Delta\theta$, even at SNR $= -20$ dB. Similar improvement on precision was observed in the literature of FDA [55], [53]. In [55],

doi:10.6342/NTU202302364

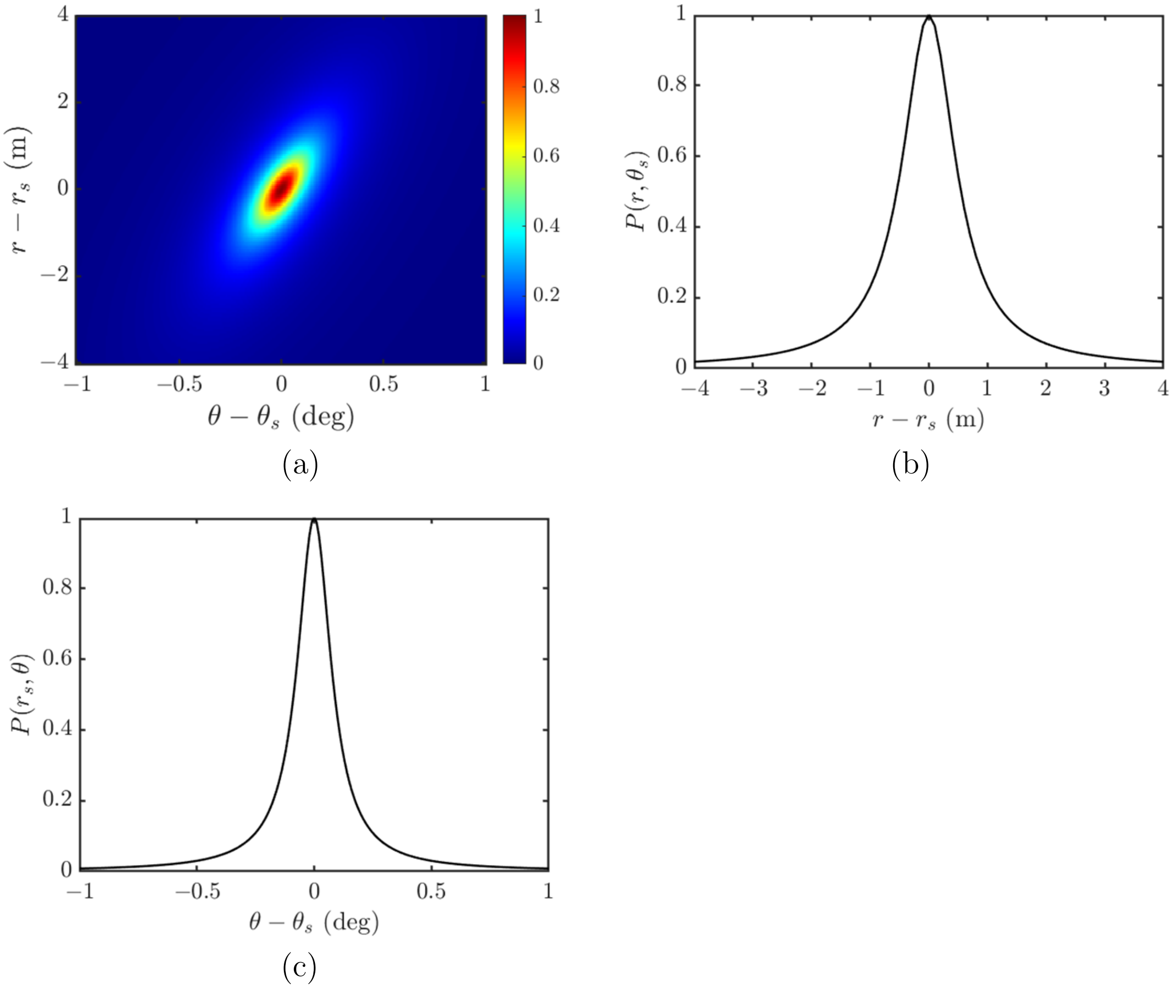

Figure 6.4: MVDR spectrum in target range-azimuth cell, centered at $r_s = 50$ km, $\theta_s = 0°$, (a) two-dimensional spectrum, (b) spectrum at $\theta_s = 0°$, (c) spectrum at $r_s = 50$ km, SNR = 10 dB.

the number of transmit-array elements is 10, leading to $\Delta\theta = 10°$. The simulation results in Fig.10 of [55] shows that $(\delta\theta)^2 = 0.5$ at SNR $= -20$ dB, which implies $\delta\theta/\Delta\theta \simeq 0.07$. In [53], the number of transmit-array elements is 8, leading to $\Delta\theta = 12.5°$. The simulation results in Fig.4 of [53] shows that $(\delta\theta)^2 = 0.7$ at SNR $= -20$ dB, which implies $\delta\theta/\Delta\theta \simeq 0.07$.

Since the frequency diverse scheme only affects the range resolution, the azimuth properties of FD-MIMO array are the same as those of MIMO array of the same physical length.

doi:10.6342/NTU202302364

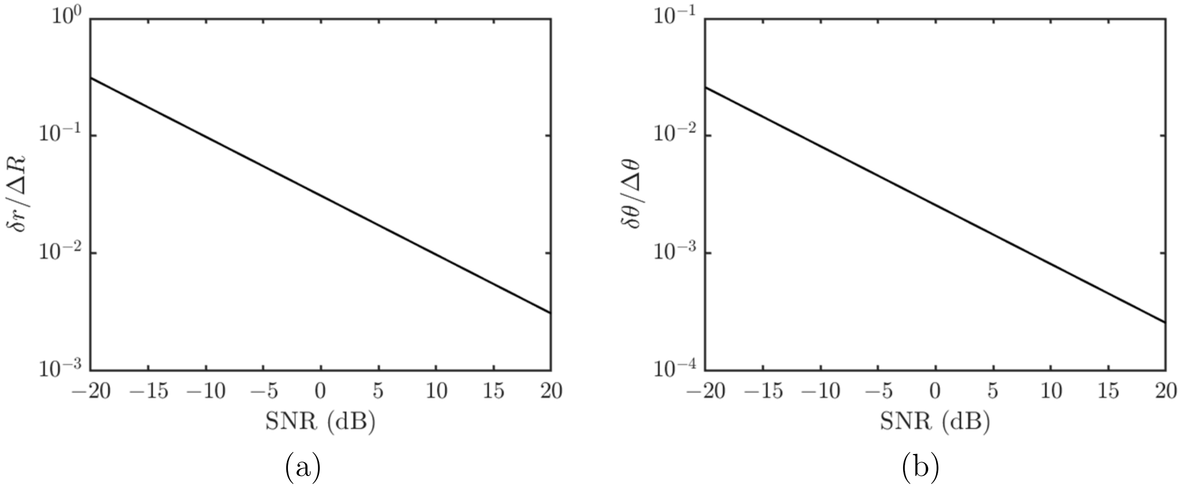

Figure 6.5: Ratio of (a) $\delta r/\Delta r$ and (b) $\delta\theta/\Delta\theta$ versus SNR.

The CRBs on estimating the direction-of-arrival (DOA) with FD-MIMO and MIMO arrays are also the same [82]-[84].

6.1 Highlight of Contributions

The main contributions of this work are summarized as follows.

1. We propose for the first time a novel FH-LFM-FD-MIMO radar system to counter false-target jamming. The proposed system inherits the merits of frequency hopping (FH) scheme and FD-MIMO array to suppress jamming signals in both frequency and spatial domains. The proposed system proves more effective than conventional countermeasures by simulations.

2. The frequency-diverse codebook for implementing the FH scheme is generated by combining a particle swarm optimization (PSO) algorithm and a rank-order-value (ROV)

doi:10.6342/NTU202302364

mapping, effectively suppressing jamming signals carrying different FD codes.

3. By adopting linear frequency modulation (LFM) waveform in an FD-MIMO array, spotlight response with low sidelobe level is achieved.
4. The spotlight-range beamforming vector is fine-tuned with a second PSO algorithm to further reduce the sidelobe level of spotlight response.
5. A detection scheme is proposed by applying frequency-hopping (FH) scheme to the FD codes in a sequence of PRIs to increase the overall detection probability, under constant false-alarm rate. Binary integration is adopted to counter more severe jamming pattern.
6. A two-dimensional MVDR spectrum is applied on the target range-azimuth cell to further enhance the localization precision.

Chapter 7

Conclusions

A novel FH-LFM-FD-MIMO radar system is proposed to counter false-target jamming. The combination of frequency-hopping scheme and spotlight response of the LFM-FD-MIMO array can suppress jamming signals more effectively than conventional countermeasures. Simulations verify that the jamming signals at the center of the spotlight response are suppressed by more than 20 dB compared to conventional approaches. The detection probability is improved by raising the signal-to-noise-plus-jamming ratio after processing the received signals. A two-step localization scheme is proposed by first detecting a target in specific range-azimuth cell with the spotlight response of the proposed scheme, then applying a two-dimensional MVDR spectrum to pinpoint the target at a much finer resolution restricted by the SNR of the received signals at each receive-array element.

doi:10.6342/NTU202302364

Bibliography

[1] W. Liu, J. Liu, X. Hu, Z. Tang, L. Huang and Y. -L. Wang, “Statistical performance analysis of the adaptive orthogonal rejection detector,” *IEEE Signal Processing Lett.*, vol. 23, no. 6, pp. 873-877, June 2016, doi: 10.1109/LSP.2016.2550495.

[2] P. Sharma, K. K. Sarma and N. E. Mastorakis, “Artificial intelligence aided electronic warfare systems- Recent trends and evolving applications,” *IEEE Access*, vol. 8, pp. 224761-224780, 2020, doi: 10.1109/ACCESS.2020.3044453.

[3] M. Tan, C. Wang, B. Xue and J. Xu, “A novel deceptive jamming approach against frequency diverse array radar,” *IEEE Sensors J.*, vol. 21, no. 6, pp. 8323-8332, March 15, 2021, doi: 10.1109/JSEN.2020.3045757.

[4] S. D. Berger, “Digital radio frequency memory linear range gate stealer spectrum,” *IEEE Trans. Aerospace Electronic Syst.*, vol. 39, no. 2, pp. 725-735, April 2003, doi: 10.1109/TAES.2003.1207279.

[5] F. A. Butt, I. H. Naqvi and A. I. Najam, "Radar ECCM against deception jamming: A novel approach using bi-static and mono-static radars," *Int. Multitopic Conf. (INMIC)*, 2012, pp. 137-141, doi: 10.1109/INMIC.2012.6511482.

[6] D. Feng, L. Xu, X. Pan and X. Wang, "Jamming wideband radar using interrupted-sampling repeater," *IEEE Trans. Aerospace Electronic Syst.*, vol. 53, no. 3, pp. 1341-1354, June 2017, doi: 10.1109/TAES.2017.2670958.

[7] P. Lingadevaru, B. Pardhasaradhi and P. Srihari, "Sequential fusion based approach for estimating range gate pull-off parameter in a networked radar system: An ECCM algorithm," *IEEE Access*, 2022, doi: 10.1109/ACCESS.2022.3185240.

[8] D. Orlando, "A novel noise jamming detection algorithm for radar applications," *IEEE Signal Processing Lett.*, vol. 24, no. 2, pp. 206-210, Feb. 2017, doi: 10.1109/LSP.2016.2645793.

[9] J. Schuerger and D. Garmatyuk, "Deception jamming modeling in radar sensor networks," *IEEE Military Commun. Conf.*, 2008, pp. 1-7, doi: 10.1109/MILCOM.2008.4753118.

[10] J. Chen, S. Xu, J. Zou and Z. Chen, "Interrupted-sampling repeater jamming suppression based on stacked bidirectional gated recurrent unit network and infinite training,"

doi:10.6342/NTU202302364

IEEE Access, vol. 7, pp. 107428-107437, 2019, doi: 10.1109/ACCESS.2019.2932793.

[11] J. D. Zhang, X. H. Zhu and K. Wang, "A waveform diversity technique for countering RGPO," *IET Int. Radar Conf.*, 2009, pp. 1-4, doi: 10.1049/cp.2009.0213.

[12] S. Zhang, Y. Yang, G. Cui, B. Wang, H. Ji and S. Iommelli, "Range-velocity jamming suppression algorithm based on adaptive iterative filtering," *IEEE Radar Conf.*, 2016, pp. 1-6, doi: 10.1109/RADAR.2016.7485305.

[13] J. Zhang, D. Zhu and G. Zhang, "New antivelocity deception jamming technique using pulses with adaptive initial phases," *IEEE Trans. Aerospace Electronic Syst.*, vol. 49, no. 2, pp. 1290-1300, April 2013, doi: 10.1109/TAES.2013.6494414.

[14] Y. Yang, J. Wu, G. L. Cui, L. Li, L. J. Kong and Y. L. Huang, "Optimized phase-coded waveform design against velocity deception," *IEEE Radar Conf.*, 2015, pp. 0400-0404, doi: 10.1109/RADAR.2015.7131032.

[15] M. Soumekh, "SAR-ECCM using phase-perturbed LFM chirp signals and DRFM repeat jammer penalization," *IEEE Trans. Aerospace Electronic Syst.*, vol. 42, no. 1, pp. 191-205, Jan. 2006, doi: 10.1109/TAES.2006.1603414.

[16] J. Akhtar, “An ECCM scheme for orthogonal independent range-focusing of real and false targets,” *IEEE Radar Conf.*, 2007, pp. 846-849, doi: 10.1109/RADAR.2007.374330.

[17] J. Akhtar, “Orthogonal block coded ECCM schemes against repeat radar jammers,” *IEEE Trans. Aerospace Electronic Syst.*, vol. 45, no. 3, pp. 1218-1226, July 2009, doi: 10.1109/TAES.2009.5259195.

[18] Y. Li, T. Huang, X. Xu, Y. Liu, L. Wang and Y. C. Eldar, “Phase transitions in frequency agile radar using compressed sensing,” *IEEE Trans. Signal Processing*, vol. 69, pp. 4801-4818, 2021, doi: 10.1109/TSP.2021.3099629.

[19] S. Wei, L. Zhang and H. Liu, “Joint frequency and PRF agility waveform optimization for high-resolution ISAR imaging,” *IEEE Trans. Geosci. Remote Sensing*, vol. 60, pp. 1-23, 2022, Art no. 5100723, doi: 10.1109/TGRS.2021.3051038.

[20] Y. Quan, Y. Wu, Y. Li, G. Sun, M. Xing, “Range-Doppler reconstruction for frequency agile and PRF-jittering radar,” *IET Radar Sonar Navig.*, vol. 12, no.3, pp. 348-352, 2018.

[21] L. Lan, *et al.* “Mainlobe deceptive jammer suppression using element-pulse coding with MIMO radar,” *Signal Processing* 182, 107955, 2021.

[22] A. de Maio, A. Farina and F. Gini, “Performance analysis of the sidelobe blanking system for two fluctuating jammer models,” *IEEE Trans. Aerospace Electronic Syst.*, vol. 41, no. 3, pp. 1082-1091, July 2005, doi: 10.1109/TAES.2005.1541453.

[23] U. Nickel, “Design of generalised 2D adaptive sidelobe blanking detectors using the detection margin,” *Signal Processing*, vol. 90, pp. 1357-1372, May 2010.

[24] O. G. Vendik and D. S. Kozlov, “Phased antenna array with a sidelobe cancellation for suppression of jamming,” *IEEE Antennas Wireless Propagat. Lett.*, vol. 11, pp. 648-650, 2012, doi: 10.1109/LAWP.2012.2203780.

[25] S. Zhao, L. Zhang, Y. Zhou and N. Liu, “Signal fusion-based algorithms to discriminate between radar targets and deception jamming in distributed multiple-radar architectures,” *IEEE Sensors J.*, vol. 15, no. 11, pp. 6697-6706, Nov. 2015, doi: 10.1109/JSEN.2015.2440769.

[26] Q. Li, L. Zhang, Y. Zhou, S. Zhao, N. Liu and J. Zhang, “Discrimination of active false targets based on hermitian distance for distributed multiple-radar architectures,” *IEEE Access*, vol. 7, pp. 71872-71883, 2019, doi: 10.1109/ACCESS.2019.2920365.

[27] P. F. Sammartino, C. J. Baker and H. D. Griffiths, “Frequency diverse MIMO techniques for radar,” *IEEE Trans. Aerospace Electronic Syst.*, vol. 49, no. 1, pp. 201-222, Jan.

doi:10.6342/NTU202302364

2013, doi: 10.1109/TAES.2013.6404099.

[28] W. -Q. Wang, "Overview of frequency diverse array in radar and navigation applications," *IET Radar Sonar Navig.*, vol. 10, 2016.

[29] G. Li, Q. Zhang, Y. Luo, K. Li, L. Su and R. Li, "An anti-jamming method of ISAR imaging with FDA-MIMO radar," *IEEE Sensor Array and Multichannel Signal Processing Workshop (SAM)*, 2018, pp. 490-493, doi: 10.1109/SAM.2018.8448422.

[30] Y. Liu, C. Wang, J. Gong and G. Chen, "Discrimination of mainlobe deceptive target with meter-wave FDA-MIMO radar," *IEEE Commun. Lett.*, vol. 26, no. 5, pp. 1131-1135, May 2022, doi: 10.1109/LCOMM.2022.3155371.

[31] W. -Q. Wang, H. C. So and A. Farina, "FDA-MIMO signal processing for mainlobe jammer suppression," *Euro. Signal Processing Conf.*, 2019, pp. 1-5, doi: 10.23919/EUSIPCO.2019.8902536.

[32] W. Wang, "Range-angle dependent transmit beampattern synthesis for linear frequency diverse arrays," *IEEE Trans. Antennas Propagat.*, vol. 61, no. 8, pp. 4073-4081, Aug. 2013, doi: 10.1109/TAP.2013.2260515.

[33] W. Khan, I. M. Qureshi and S. Saeed, “Frequency diverse array radar with logarithmically increasing frequency offset,” *IEEE Antennas Wireless Propagat. Lett.*, vol. 14, pp. 499-502, 2015, doi: 10.1109/LAWP.2014.2368977.

[34] Y. Liao, W. Wang and Z. Zheng, “Frequency diverse array beampattern synthesis using symmetrical logarithmic frequency offsets for target indication,” *IEEE Trans. Antennas Propagat.*, vol. 67, no. 5, pp. 3505-3509, May 2019, doi: 10.1109/TAP.2019.2900353.

[35] A. Basit, I. M. Qureshi, W. Khan, S. u. Rehman and M. M. Khan, “Beam pattern synthesis for an FDA radar with Hamming window-based nonuniform frequency offset,” *IEEE Antennas Wireless Propagat. Lett.*, vol. 16, pp. 2283-2286, 2017, doi: 10.1109/LAWP.2017.2714761.

[36] Y. Liao, H. Tang, X. Chen and W. -Q. Wang, “Frequency diverse array beampattern synthesis with Taylor windowed frequency offsets,” *IEEE Antennas Wireless Propagat. Lett.*, vol. 19, no. 11, pp. 1901-1905, Nov. 2020, doi: 10.1109/LAWP.2020.3024710.

[37] H. Shao, J. Dai, J. Xiong, H. Chen and W. Wang, “Dot-shaped range-angle beampattern synthesis for frequency diverse array,” *IEEE Antennas Wireless Propagat. Lett.*, vol. 15, pp. 1703-1706, 2016, doi: 10.1109/LAWP.2016.2527818.

doi:10.6342/NTU202302364

[38] Y. Xu, X. Shi, W. Li and J. Xu, “Flat-top beampattern synthesis in range and angle domains for frequency diverse array via second-order cone programming,” *IEEE Antennas Wireless Propagat. Lett.*, vol. 15, pp. 1479-1482, 2016, doi: 10.1109/LAWP.2015.2513758.

[39] J. Xiong, W. Wang, H. Shao and H. Chen, “Frequency diverse array transmit beampattern optimization with genetic algorithm,” *IEEE Antennas Wireless Propagat. Lett.*, vol. 16, pp. 469-472, 2017, doi: 10.1109/LAWP.2016.2584078.

[40] Y. Liao, J. Wang and Q. H. Liu, “Transmit beampattern synthesis for frequency diverse array with particle swarm frequency offset optimization,” *IEEE Transactions Antennas Propagat.*, vol. 69, no. 2, pp. 892-901, Feb. 2021, doi: 10.1109/TAP.2020.3027576.

[41] J. Xu, G. Liao, L. Huang and H. C. So, “Robust adaptive beamforming for fast-moving target detection with FDA-STAP radar,” *IEEE Trans. Signal Processing*, vol. 65, no. 4, pp. 973-984, 15 Feb.15, 2017, doi: 10.1109/TSP.2016.2628340.

[42] L. Lan *et al.*, “GLRT-based adaptive target detection in FDA-MIMO radar,” *IEEE Trans. Aerospace Electronic Syst.*, vol. 57, no. 1, pp. 597-613, Feb. 2021, doi: 10.1109/TAES.2020.3028485.

doi:10.6342/NTU202302364

[43] B. Huang, J. Jian, A. Basit, R. Gui and W. -Q. Wang, “Adaptive distributed target detection for FDA-MIMO radar in Gaussian clutter without training data,” *IEEE Trans. Aerospace Electronic Syst.*, vol. 58, no. 4, pp. 2961-2972, Aug. 2022, doi: 10.1109/TAES.2022.3145781.

[44] B. Huang, W. -Q. Wang, A. Basit and R. Gui, “Bayesian detection in Gaussian clutter for FDA-MIMO radar,” *IEEE Trans. Veh. Technol.*, vol. 71, no. 3, pp. 2655-2667, March 2022, doi: 10.1109/TVT.2021.3139894.

[45] B. Huang, A. Basit, W. -Q. Wang and S. Zhang, “Adaptive detection with Bayesian framework for FDA-MIMO radar,” *IEEE Geosci. Remote Sensing Lett.*, vol. 19, pp. 1-5, 2022, Art no. 3509505, doi: 10.1109/LGRS.2021.3123654.

[46] B. Huang, A. Basit, R. Gui and W. -Q. Wang, “Adaptive moving target detection without training data for FDA-MIMO radar,” *IEEE Trans. Veh. Technol.*, vol. 71, no. 1, pp. 220-232, Jan. 2022, doi: 10.1109/TVT.2021.3126781.

[47] X. Chen, B. Chen, J. Guan, Y. Huang and Y. He, “Space-range-doppler focus-based low-observable moving target detection using frequency diverse array MIMO radar,” *IEEE Access*, vol. 6, pp. 43892-43904, 2018, doi: 10.1109/ACCESS.2018.2863745.

[48] Z. Ding and J. Xie, “Joint transmit and receive beamforming for cognitive FDA-MIMO radar with moving target,” *IEEE Sensors J.*, vol. 21, no. 18, pp. 20878-20885, 15 Sept.15, 2021, doi: 10.1109/JSEN.2021.3100332.

[49] Y. Zhu, L. Liu, Z. Lu and S. Zhang, “Target detection performance analysis of FDA-MIMO radar,” *IEEE Access*, vol. 7, pp. 164276-164285, 2019, doi: 10.1109/ACCESS.2019.2943082.

[50] F. Wen, J. Shi, J. He and T. -K. Truong, “2D-DoD and 2D-DoA estimation using sparse L-shaped EMVS-MIMO radar,” *IEEE Trans. Aerospace Electronic Syst.*, vol. 59, no. 2, pp. 2077-2084, April 2023, doi: 10.1109/TAES.2022.3208858.

[51] J. Wang, P. Wang, F. Luo and W. Wu, “Waveform design and DoA-DoD estimation of OFDM-LFM signal based on SDFnT for MIMO radar,” *IEEE Access*, vol. 11, pp. 1348-1358, 2023, doi: 10.1109/ACCESS.2022.3233103.

[52] Y. -C. Lin and T. -S. Lee, “Max-MUSIC: A low-complexity high-resolution direction finding method for sparse MIMO radars,” *IEEE Sensors J.*, vol. 20, no. 24, pp. 14914-14923, 15 Dec.15, 2020, doi: 10.1109/JSEN.2020.3009426.

[53] J. Xiong, W. -Q. Wang and K. Gao, “FDA-MIMO radar range-angle estimation: CRLB, MSE, and resolution analysis,” *IEEE Trans. Aerospace Electronic Syst.*, vol. 54, no. 1,

pp. 284-294, Feb. 2018, doi: 10.1109/TAES.2017.2756498.

[54] C. Wen, J. Peng, Y. Zhou and J. Wu, “Enhanced three-dimensional joint domain localized STAP for airborne FDA-MIMO radar under dense false-target jamming scenario,” *IEEE Sensors J.*, vol. 18, no. 10, pp. 4154-4166, May 15, 2018, doi: 10.1109/JSEN.2018.2820905.

[55] J. Xu, G. Liao, S. Zhu, L. Huang and H. C. So, “Joint range and angle estimation using MIMO radar with frequency diverse array,” *IEEE Trans. Signal Processing*, vol. 63, no. 13, pp. 3396-3410, July 2015, doi: 10.1109/TSP.2015.2422680.

[56] Yao, W. Wu and D. Fang, “Frequency diverse array antenna using time-modulated optimized frequency offset to obtain time-invariant spatial fine focusing beampattern,” *IEEE Trans. Antennas Propagat.*, vol. 64, no. 10, pp. 4434-4446, Oct. 2016, doi: 10.1109/TAP.2016.2594075.

[57] W. Khan and I. M. Qureshi, “Frequency diverse array radar with time-dependent frequency offset,” *IEEE Antennas Wireless Propagat. Lett.*, vol. 13, pp. 758-761, 2014, doi: 10.1109/LAWP.2014.2315215.

[58] Y. Wang, W. Li, G. Huang and J. Li, “Time-invariant range-angle-dependent beampattern synthesis for FDA radar targets tracking,” *IEEE Antennas Wireless Propagat.*

Lett., vol. 16, pp. 2375-2379, 2017, doi: 10.1109/LAWP.2017.2718580.

[59] K. Chen, S. Yang, Y. Chen and S. Qu, “Accurate models of time-invariant beampatterns for frequency diverse arrays,” *IEEE Trans. Antennas Propagat.*, vol. 67, no. 5, pp. 3022-3029, May 2019, doi: 10.1109/TAP.2019.2896712.

[60] M. Tan, C. Wang and Z. Li, “Correction analysis of frequency diverse array radar about time,” *IEEE Trans. Antennas Propagat.*, vol. 69, no. 2, pp. 834-847, Feb. 2021, doi: 10.1109/TAP.2020.3016508.

[61] Y. Xu, X. Shi, W. Li, J. Xu and L. Huang, “Low-sidelobe range-angle beamforming with FDA using multiple parameter optimization,” *IEEE Trans. Aerospace Electronic Syst.*, vol. 55, no. 5, pp. 2214-2225, Oct. 2019, doi: 10.1109/TAES.2018.2883873.

[62] Y. Xu and K. Luk, “Enhanced transmit-receive beamforming for frequency diverse array,” *IEEE Trans. Antennas Propagat.*, vol. 68, no. 7, pp. 5344-5352, July 2020, doi: 10.1109/TAP.2020.2977717.

[63] Y. Xu, A. Wang and J. Xu, “Range-angle transceiver beamforming based on semicircular-FDA scheme,” *IEEE Trans. Aerospace Electronic Syst.*, vol. 58, no. 2, pp. 834-843, April 2022, doi: 10.1109/TAES.2021.3111792.

[64] J. Xu, J. Kang, G. Liao and H. C. So, "Mainlobe deceptive jammer suppression with FDA-MIMO radar," *IEEE Sensor Array and Multichannel Signal Processing Workshop (SAM)*, 2018, pp. 504-508, doi: 10.1109/SAM.2018.8448961.

[65] L. Lan, G. Liao, J. Xu, Y. Zhang and F. Fioranelli, "Suppression approach to main-beam deceptive jamming in FDA-MIMO radar using nonhomogeneous sample detection," *IEEE Access*, vol. 6, pp. 34582-34597, 2018, doi: 10.1109/ACCESS.2018.2850816.

[66] M. Akcakaya and A. Nehorai, "MIMO radar sensitivity analysis for target detection," *IEEE Trans. Signal Processing*, vol. 59, no. 7, pp. 3241-3250, July 2011, doi: 10.1109/TSP.2011.2141665.

[67] J. Xu, S. Zhu and G. Liao, "Space-time-range adaptive processing for airborne radar systems," *IEEE Sensors J.*, vol. 15, no. 3, pp. 1602-1610, March 2015, doi: 10.1109/JSEN.2014.2364594.

[68] Z. Ding, J. Xie, B. Wang and H. Zhang, "Robust adaptive null broadening method based on FDA-MIMO radar," *IEEE Access*, vol. 8, pp. 177976-177983, 2020, doi: 10.1109/ACCESS.2020.3025602.

[69] H. He, P. Stoica and J. Li, "Designing unimodular sequence sets with good correlations-Including an application to MIMO radar," *IEEE Trans. Signal Processing*, vol. 57, no.

11, pp. 4391-4405, Nov. 2009, doi: 10.1109/TSP.2009.2025108.

[70] L. Lan, G. Liao, J. Xu, Y. Zhang and B. Liao, “Transceive beamforming with accurate nulling in FDA-MIMO radar for imaging,” *IEEE Trans. Geosci. Remote Sensing*, vol. 58, no. 6, pp. 4145-4159, June 2020, doi: 10.1109/TGRS.2019.2961324.

[71] L. Lan, J. Xu, G. Liao, Y. Zhang, F. Fioranelli and H. C. So, “Suppression of mainbeam deceptive jammer with FDA-MIMO radar,” *IEEE Trans. Veh. Technol.*, vol. 69, no. 10, pp. 11584-11598, Oct. 2020, doi: 10.1109/TVT.2020.3014689.

[72] R. Gui, W. -Q. Wang and H. Shao, “General receiver design for FDA radar,” *IEEE Radar Conf.*, 2018, pp. 0280-0285, doi: 10.1109/RADAR.2018.8378571.

[73] B. Liu, L. Wang and Y. Jin, “An effective PSO-based memetic algorithm for flow shop scheduling,” *IEEE Trans. Systems, Man, Cybernetics, Part B*, vol. 37, no. 1, pp. 18-27, Feb. 2007, doi: 10.1109/TSMCB.2006.883272.

[74] M. Clerc and J. Kennedy, “The particle swarm-explosion, stability, and convergence in a multidimensional complex space,” *IEEE Trans. Evol. Comput.*, vol. 6, no. 1, pp. 58-73, Feb. 2002, doi: 10.1109/4235.985692.

[75] G. W. Stimson, *Introduction to Airborne Radar*, 2nd ed., SciTech Publishing, 1998.

doi:10.6342/NTU202302364

[76] F. Gini, A. De Maio and L. Patton, *Waveform Design and Diversity for Advanced Radar Systems*, London: Institution of Engineering and Technology, 2012.

[77] R. Gui, B. Huang, W. -Q. Wang and Y. Sun, “Generalized ambiguity function for FDA radar joint range, angle and Doppler resolution evaluation,” *IEEE Geosci. Remote Sensing Lett.*, vol. 19, pp. 1-5, 2022, Art no. 3502305, doi: 10.1109/LGRS.2020.3044351.

[78] M. A. Richards, *Fundamentals of Radar Signal Processing*, New York: McGraw-Hill, 2005.

[79] L. Tzafri and A. J. Weiss, “High-resolution direct position determination Using MVDR,” *IEEE Trans. Wireless Commun.*, vol. 15, no. 9, pp. 6449-6461, Sept. 2016, doi: 10.1109/TWC.2016.2585116.

[80] Y. Guo, G. Liao, Q. Zhang, J. Li and T. Gu, “A robust radial velocity estimation method for FDA-SAR,” *IEEE Geosci. Remote Sensing Lett.*, vol. 17, no. 4, pp. 646-650, April 2020, doi: 10.1109/LGRS.2019.2929493.

[81] R. Guo, Y. Ni, H. Liu, F. Wang and L. He, “Signal diverse array radar for electronic warfare,” *IEEE Antennas Wireless Propagat. Lett.*, vol. 16, pp. 2906-2910, 2017, doi: 10.1109/LAWP.2017.2751648.

[82] H. Lee and J. Chun, “Virtual array response vector for angle estimation of MIMO radar with a wide-band interleaved OFDM signal,” *IEEE Commun. Lett.*, vol. 25, no. 5, pp. 1539-1543, May 2021, doi: 10.1109/LCOMM.2021.3049355.

[83] A. H. Shaikh, X. Dang, T. Ahmed and D. Huang, “New transmit-receive array configurations for the MIMO radar with enhanced degrees of freedom,” *IEEE Commun. Lett.*, vol. 24, no. 7, pp. 1534-1538, July 2020, doi: 10.1109/LCOMM.2020.2983403.

[84] Z. Huang, X. Li, P. Huang and W. Wang, “2-D DOA estimation for incoherently distributed sources considering mixed circular and noncircular signals in massive MIMO system,” *IEEE Access*, vol. 7, pp. 106900-106911, 2019, doi: 10.1109/ACCESS.2019.2932004.